TOPICAL REVIEW

Condensation and pattern formation in cold exciton gases in coupled quantum wells

L V Butov

Department of Physics, University of California at San Diego, San Diego, CA, USA

Abstract
Bound electron–hole pairs—excitons—are light Bose particles with a mass
comparable to or smaller than that of the free electron. Since the quantum
degeneracy temperature scales inversely with the mass, it is anticipated that
Bose–Einstein condensation of an exciton gas can be achieved at temperatures
of about 1 K, orders of magnitude larger than the micro-Kelvin temperatures
employed in atomic condensation. High quantum degeneracy temperatures and
the possibility to control exciton density by laser photoexcitation make cold
excitons a model system for studies of collective states and many-body
phenomena in a system of cold bosons. Experimentally, an exciton temperature
well below 1 K is achieved in a gas of indirect excitons in coupled quantum-
well semiconductor heterostructures. Here, we overview phenomena in the cold
exciton gases: condensation, pattern formation, and macroscopically ordered
exciton states.

(Some figures in this article are in colour only in the electronic version.)

1. Introduction: problem of exciton condensation

An exciton is an electron–hole bound pair in a semiconductor. More than three decades ago
Keldysh and Kozlov [72] showed that in the dilute limit ($n a_B{}^D \ll 1$, where a_B is the exciton
Bohr radius, n the exciton density, and D the dimensionality) excitons are weakly interacting
Bose particles and are expected to undergo Bose–Einstein condensation (BEC). Because the
exciton mass, M_X, is small—even smaller than the free electron mass—exciton condensation
should occur at temperatures of about 1 K for experimentally accessible exciton densities,
several orders of magnitude higher than for atoms. The discovery of atomic BEC is reviewed
in [36, 75]. In the opposite limit of a dense e–h system ($n a_B{}^D \gg 1$) excitons are analogous
to Cooper pairs and the exciton condensate, called the excitonic insulator, is analogous to
the BCS superconductor state [71]. Contrary to the BCS superconductor state, the pairing
in the excitonic insulator is due to electron–hole interaction, the pairs are neutral and the
state is insulating. For exciton condensation in a dense electron–hole system, the nesting of
the electron and hole Fermi-surfaces is required. The nature of the exciton condensation is

different in these two limits. In the case of BEC of excitons in the low-density limit, excitons exist well above the critical temperature, the number of excitons is fixed and does not change at the critical temperature, and the critical temperature for exciton condensation is determined by the statistical distribution in momentum space of weakly interacting bosons (i.e. excitons) [72], see below. In contrast, in the case of BCS-like condensation of excitons in the high-density limit, excitons are formed at the critical temperature and the critical temperature for exciton condensation is determined by a pairing similar to the case of Cooper pairs [71]. The transition between the dilute and the dense limit is smooth and the condensation has a mixed nature for intermediate densities $na_B^D \sim 1$ [71, 35, 110].

In spite of the relatively high critical temperature, T_c, it is experimentally challenging to lower the temperature of an exciton gas enough to reach exciton condensation. Cooling semiconductor lattices well below $1\,K$ is routinely achieved with He-refrigerators. Nevertheless, the exciton temperature, T_X, is determined by the ratio of the exciton energy relaxation and recombination rates and can considerably exceed that of the lattice. In order to create a cold exciton gas with T_X close to the lattice temperature, the exciton lifetime should considerably exceed the exciton energy relaxation time.

In addition, for the observation of exciton condensation, the semiconductors in which the exciton condensate is a ground state, in particular, requires a lower energy than the metallic electron–hole liquid. The electron–hole liquid is a real space condensate and is the ground state in Ge and Si that is the main obstacle for the creation of cold and dense exciton gases in these materials [73].

Over the last two decades, experimental efforts to observe exciton BEC in bulk semiconductors dealt mainly with bulk Cu_2O [64, 123, 124, 62, 50, 96, 103, 58, 111, 112, 142, 113], a material whose ground exciton state is optically dipole-inactive and has, therefore, a low radiative recombination rate. The conditions necessary for the realization of BEC in Cu_2O appeared to be experimentally accessible: $T_{c-3D} = 0.527 \cdot 2\pi\hbar^2/(M_X h_B)(n/g)^{2/3}$ (g is the spin degeneracy of the exciton state and h_B is the Boltzmann constant) would reach $\cong 2.3\,K$ at exciton density $n = 10^{17}\,cm^{-3}$. Many phenomena in exciton transport and photoluminescence (PL) have been observed in exciton gases in Cu_2O, in particular: expansion of the front of the exciton cloud at near-sonic velocity, which was discussed in terms of the exciton condensate superfluidity [124]; a reduction in the velocity dispersion of excitons, which was discussed in terms of the motion of an exciton superfluid in the form of a quasi-stable wave packet with little spatial dispersion [50]; an amplification of a directed beam of excitons, which was discussed in terms of stimulated exciton scattering [103]; and an enhancement of PL intensity at low energies compared to that for the Maxwell–Boltzmann exciton distribution, which was discussed in terms of the Bose–Einstein distribution of excitons [64, 123] and the PL of the exciton Bose–Einstein condensate [96, 58]. However, another competitive density-dependent process turns on at high n: the exciton Auger recombination rate, $\sim n$, which increases faster than T_c with increasing n. Auger recombination depletes the exciton gas and results in its heating. Recent measurements indicate that the Auger recombination rate in Cu_2O is about two orders of magnitude higher than was assumed before and, therefore, the exciton densities reached in the up-to-date experiments are far below that required to achieve a degenerate Bose-gas of excitons [111, 112, 142, 113]. These measurements suggest alternative interpretations for the phenomena in exciton gases in Cu_2O. In particular, the transport experiments were interpreted in terms of the phonon wind effect as the mechanism which moves the exciton cloud at nearly the sound velocity, an explanation that does not depend on Bose statistics of the excitons [11, 135, 136], while the data on the PL lineshape were explained by spatial inhomogeneity of the classical exciton gas [111, 112, 142, 113]. Searches for exciton condensation in Cu_2O are, at present, in progress, see e.g. [104].
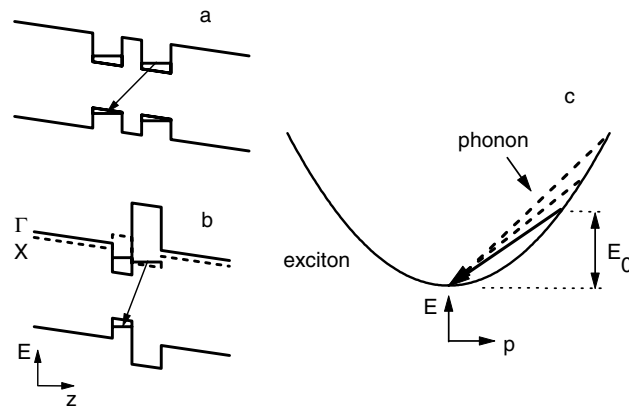
Figure 1. Energy band diagram of GaAs/AlGaAs (a) and AlAs/GaAs (b) CQWs. The indirect transition is indicated by the arrow. (c) Energy diagram for the LA-phonon-assisted relaxation for bulk excitons (solid arrow) and for QW excitons (solid and dashed arrows).

The experimental efforts to observe the exciton condensation in bulk semiconductors dealt also with uniaxially strained Ge where the stability of the electron–hole liquid is reduced by the strain. Fitting the PL lineshape to the Bose–Einstein distribution was discussed for excitons in uniaxially strained Ge [81, 137].

Because of the long lifetime and high cooling rate, the indirect excitons in CQWs form a system where a cold exciton gas can be created. The long lifetimes are due to the spatial separation of the electron and hole wells [97, 122, 51], resulting in a radiative lifetime of indirect excitons in CQW samples that is more than three orders of magnitude longer than that of direct excitons in single QWs. The cooling of hot photoexcited excitons down to the temperatures of the cold lattice, which occurs via emission of bulk LA phonons, is about three orders of magnitude faster for excitons in GaAs QWs than that in bulk GaAs. This is due to relaxation of the momentum conservation law in a direction perpendicular to the QW plane. Indeed, for quasi-2D systems, the ground-state mode $E = 0$ couples to the continuum of the energy states $E \geqslant E_0$, rather than to the single energy state $E = E_0 = 2Mv_s^2$ (v_s is the sound velocity) as occurs in bulk semiconductors [133, 134, 66, 145, 67] (figure 1(c)).

A necessary requirement for BEC is the thermal distribution of bosons. Indeed, the thermal distribution is the basis of the BEC phenomenon: at thermal equilibrium above T_c, the distribution of all bosons obeys the Bose–Einstein distribution function $f(E) = 1/(\exp[(E - \mu)/k_B T] - 1)$ while below T_c all particles cannot follow the Bose–Einstein distribution and, according to the Einstein hypothesis, a finite fraction of all the bosons occupies the same one-particle state forming the Bose–Einstein condensate. Note that the macroscopic occupation of a single state is also possible in bosonic systems without thermal distribution with the laser presenting a typical example; in this case, the macroscopic occupation of a single state is apparently different from BEC. In this respect, we note that the lifetimes of the indirect excitons are in the range from tens of nanoseconds to milliseconds and are much longer than the exciton thermalization time, which is in the subnanosecond range for free excitons [67] (for peculiarities of the exciton thermalization in the presence of an in-plane random potential see section 2.3). Therefore, the system of free indirect excitons is characterized by the established temperature and the exciton distribution is thermal.

The excitons, initially photogenerated, are hot; however, they quickly cool down to the lattice temperature, T_{lattice}, via phonon emission: e.g. the exciton temperature, T_X, can drop down to 400 mK in about 5 ns, a time much shorter than the indirect exciton lifetime

(section 3.2). Therefore, there are two ways to overcome the obstacle of hot generation and study cold gases of indirect excitons with $T_X \approx T_{lattice}$: (1) use a separation in time and study the indirect excitons a few ns after the end of the photoexcitation pulses (these experiments are overviewed in section 3.2), (2) use a separation in space and study the indirect excitons beyond the photoexcitation spot (these experiments are overviewed in section 4). In the latter case, excitons can cool down to $T_{lattice}$ as they travel away from the photoexcitation spot.

Examples of semiconductor CQWs are shown in figures 1(a) and (b). In the a-type CQWs (figure 1(a)) electrons and holes are spatially separated by a potential barrier, which provides the small overlap of electron and hole wave functions resulting in the long recombination lifetime of the indirect excitons. Different materials can be chosen for the well-barrier combination in the a-type CQWs: typical examples are the GaAs well–$Al_xGa_{1-x}As$ barrier and the $In_xGa_{1-x}As$ well–GaAs barrier. In the b-type CQWs (figure 1(b)) the effective spatial separation between electrons and holes is small compared to the a-type CQWs. The electron state in AlAs is constructed from the X minima of the conduction band. Together with the spatial separation between electrons and holes in the z direction, this results in the long lifetime of indirect excitons in the b-type CQWs. Both in the a- and b-type CQWs the exciton lifetime can be controlled by the electric field in the z-direction due to the change in the overlap of the electron and hole wavefunctions in the z-direction [1, 148, 149].

The indirect excitons are quasi-two-dimensional (2D). Below, the peculiarities of condensation in 2D systems studied in [116, 77, 9, 48, 117] are reviewed briefly. For infinite 2D systems BEC, i.e. a macroscopic occupation of the lowest energy state at finite temperatures in a system of thermally distributed bosons, does not take place. This is a consequence of the form of the 2D density of states $D_{2D}(E) = const$, which allows accumulating any amount of bosons obeying the Bose–Einstein distribution at low-energy states without condensation to the $E = 0$ state. BEC is possible for systems where the density of states goes to zero at $E = 0$, as in 3D systems with $D_{3D}(E) \sim E^{1/2}$, or in systems where the lowest energy state is separated from excited states by an energy gap, as in finite-size systems: in these systems, due to the lack of the number of states at low energies, all particles cannot follow the Bose–Einstein distribution below the critical temperature and, according to the Einstein hypothesis, a finite fraction of all the bosons occupies the lowest energy state forming the Bose–Einstein condensate.

At finite temperatures, only condensation into a superfluid state with the mean-field transition temperature $T_c \approx 2\pi\hbar^2 n/[k_B m \ln\ln(1/na^2)]$ is possible in the weakly interacting Bose gas in two dimensions (n is the density, m is the boson mass, and a is the range of interaction) [116, 9, 48]. Below T_c the small momentum particles contribute to a so-called quasi-condensate, which results in the appearance of superfluidity [116, 9, 48]. Note that the above expression for T_c is valid in the limit of the extremely dilute system when $\ln\ln(1/na^2) \gg 1$ [116, 9, 48]. For less dilute systems T_c can be approximated by $T_c \approx 2\pi\hbar^2 n/[k_B m\{\ln(\xi/4\pi) + \ln\ln(1/na^2)\}] \approx 2\pi\hbar^2 n/[k_B m \ln(\xi/4\pi)]$, where the dimensionless constant $\xi \approx 380$ [117]. The difference between the quasi-condensate and the Bose–Einstein condensate is not essential for most experiments [116, 9] and distinguishing between them unambiguously in experiments is hard (if possible), and, therefore, we do not distinguish between them by discussing the exciton condensation in the review.

One more characteristic temperature—the Kosterlitz–Thouless critical temperature—describes the pairing of free vortices in the superfluid: at $T_{KT} < T < T_c$, there are free unpaired vortices while at $T < T_{KT}$ the vortices with opposite vorticity bind to pairs. The free unpaired vortices are drawn by a flow and cause dissipation due to the movement of their normal cores. Therefore, at $T_{KT} < T < T_c$ superfluidity is local, on a characteristic length scale given by the distance between the vortices, while a macroscopic superfluid density abruptly appears at $T = T_{KT}$ [77].

For finite 2D systems, the lowest energy state is separated from excited states by an energy gap and BEC is possible as well as it is possible in any finite system like the system of atoms confined in a trap, which is explored in experiments on atomic BEC [36, 75]. The critical temperature for BEC in a finite 2D system with an area S is $T_{cS} \approx 2\pi\hbar^2 n/[k_B m \ln(nS)]$ [68, 74]. T_{cS} reduces logarithmically with the increase of the system area. The slow—logarithmic—reduction of T_{cS} makes BEC possible in real finite 2D systems (note that there are no infinite systems in solid state experiments and any experimental 3D system is a finite system as well). At the same time, $T_{cS} \to 0$ for infinite 2D systems, which is consistent with the impossibility of BEC in infinite 2D systems. Similarly, the critical temperature for BEC of bosons confined in a 2D harmonic potential trap is given by $T_c \approx \sqrt{6}/(k_B\pi)\hbar\omega\sqrt{N}$, where $\hbar\omega$ is the quantization energy and N is the number of bosons in the trap [5, 74].

Now we present the characteristic temperatures for the system of indirect excitons in a GaAs/Al$_{0.33}$Ga$_{0.67}$As CQW sample with 8 nm QWs. This sample was studied in [20–31]. For this sample, the exciton mass $M_X = 0.22m_0$ [23, 26] and the spin degeneracy of the exciton state $g = 4$ (we, therefore, substitute n by n/g in the equations for estimating the characteristic temperatures). The estimates are given for the total exciton density $n = 3 \times 10^{10}$ cm^{-2} which is well below the Mott density $n_{Mott} \sim 1/a_B^2 \sim 2 \times 10^{11}$ cm^{-2} above which the excitons dissociate due to phase-space filling and screening [121] ($a_B \sim 20$ nm for the indirect excitons [39]). The temperature T_{dB} at which the thermal de Broglie wavelength $\lambda_{dB} = \sqrt{2\pi\hbar^2/(mk_BT)}$ is comparable to the interexcitonic separation, i.e. $\lambda_{dB}^2 n/g = 1$, is given by $T_{dB} = 2\pi\hbar^2 n/(k_B M_x g) \approx 2$ K. Note that $\lambda_{dB} \approx 110$ nm at $T = 2$ K. The meaning of this temperature, as described for atoms in [75], is the following: excitons can be regarded as quantum-mechanical wave packets that have a spatial extent of the order of λ_{dB} which is the position uncertainty associated with the thermal momentum distribution; when excitons are cooled to the point where λ_{dB} is comparable to the interexcitonic separation, the excitonic wave packets 'overlap' and the gas starts to become a 'quantum soup' of indistinguishable particles (in 3D systems BEC takes place when $\lambda_{dB}^3 n = 2.612$). The temperature for the onset of quasi-condensate and local superfluidity $T_c \approx 2\pi\hbar^2 n/[k_B M_x g \ln(\xi/4\pi)] \approx 0.6$ K. The temperature of quantum degeneracy T_0, at which the occupation of the ground state $N_{E=0} = \exp(T_0/T) - 1$ is equal to one, $T_0 = \pi\hbar^2 n/(2k_B M_x g) \approx 0.5$ K [67]. The temperature for BEC in a spot of 20 μm size $T_{cS} \approx 2\pi\hbar^2 n/[k_B M_x g \ln(nS/g)] \approx 0.2$ K. These characteristic temperatures differ by a numerical factor and reflect the same physics—formation of a statistically degenerate gas of indistinguishable Bose-particles, i.e. the condensation in k-space. Note that, in the experiments reviewed below, the lowest bath temperature was 50 mK in the experiments on exciton PL kinetics and 360 mK in the experiments on pattern formation while the density was scanned in the range from $< 10^8$ cm^{-2} up to high densities corresponding to the plasma regime $> 10^{11}$ cm^{-2}, i.e. in the reviewed experiments, the excitons were studied in the range of parameters inside (deeply inside for the experiments on exciton PL kinetics) those implied by the above predictions for the condensation.

Experimental studies of the indirect excitons in CQWs form the bulk of this review. In section 2, we review the specific properties of indirect excitons in CQWs. Experimental studies of cold exciton gases and exciton condensation are reviewed in section 3 and the recently observed pattern formation in cold exciton gases is reviewed in section 4.

2. Specific properties of indirect excitons in CQW

2.1. Direct and indirect excitons in CQW

The electric field in the z direction, F, is controlled by external gate voltage V_g. In a typical CQW device, the CQW is located in an insulating intrinsic layer (with width D_i) embedded
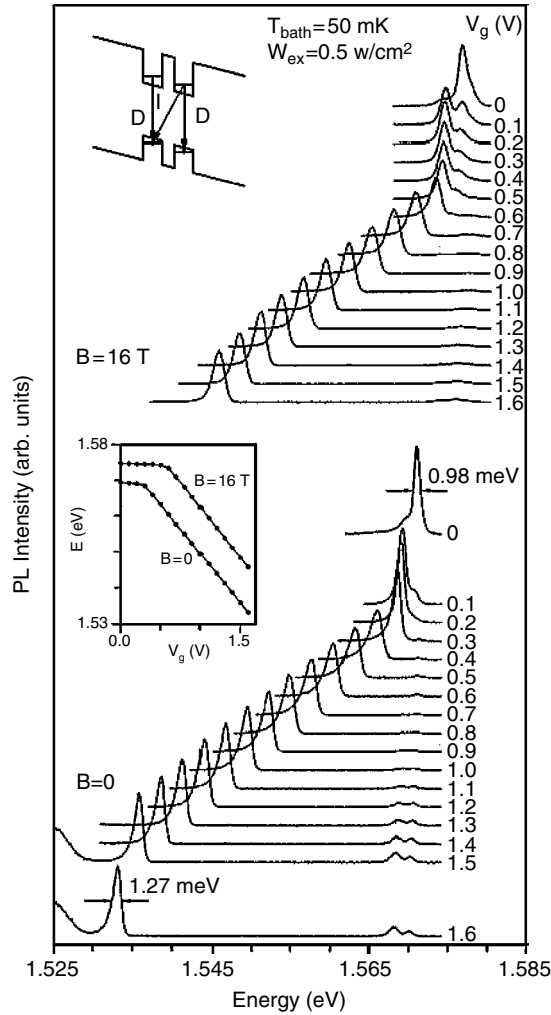
Figure 2. Gate voltage dependence of the PL spectrum at $T_{bath} = 50$ mK, $W_{ex} = 0.5$ W cm^{-2}, $B = 0$ and 16 T. Top inset: schematic band diagram of the GaAs/Al$_x$Ga$_{1-x}$As CQW structure under applied gate voltage; the direct (D) and indirect (I) exciton transitions are shown by arrows. Bottom inset: the ground-state PL line energy as a function of gate voltage. From [21].

into highly doped layers with metallic conductivity. The gate voltage is applied between the metallic cladding layers and drops entirely in the insulating layer for the properly operating device. Therefore, the electric field in the *n-i-n* samples is $F = V_g/D_i$ while that in the *p-i-n* samples is $F = F_{built-in} + V_g/D_i$, where $F_{built-in}$ is the built-in electric field in the sample (the built-in electric field in the *n-i-n* samples is close to zero). Note that the insulating character of the intrinsic layer and the metallic character of the cladding layers are essential for experiments. Otherwise, if the *i*-layer is not insulating and/or cladding layers are not metallic, F will be determined by some effective D_i^* which depends generally on parameters like temperature, excitation density, magnetic field, etc., thus introducing uncontrollable variables to the experiments and making ambiguous the data interpretation.

A typical gate-voltage dependence of the PL spectrum for the *n-i-n* GaAs/AlGaAs CQW sample is shown in figure 2 [21]. The spectra are recorded at low-excitation densities to

minimize interaction effects, which are considered in section 2.2. For positive $V_g < 0.3\,\text{V}$ the lowest energy PL line does not significantly shift with increasing V_g and has a short PL decay time (below the system resolution of 0.2 ns) and, therefore, the PL line reflects the direct exciton emission (the so-called direct regime). For higher gate voltages, the main PL line shifts linearly with increasing V_g and has a long PL decay time and thus corresponds to the indirect exciton that is constructed from the electron and hole in different QWs (the indirect regime). The ratio of the direct and indirect exciton densities in the indirect regime is proportional to the ratio between the direct and indirect PL line intensities multiplied by the ratio between the direct and indirect exciton radiative decay times and is small in the experiments (typically below 10^{-4}). The double structure of the direct exciton line in samples with equal QW widths is likely to result from the direct exciton (the higher energy line) and direct charged complexes, trions (the lower energy line) [140, 24]. For CQW samples with different QW widths the direct exciton PL energies are different for two QWs leading to additional lines in the PL spectrum. PL of cladding bulk n-GaAs layers spreads typically over tens of meV and the onset of the broad PL line corresponding to the bulk n-GaAs emission is seen at the lowest energies in figure 2. The doping level of the n-GaAs layer is typically selected to be in the range 5×10^{17}–$10^{18}\,\text{cm}^{-3}$ since the lower doping compromises the metallic conductivity of the layers while the higher doping results in a higher Fermi energy and, in turn, overlaps the bulk n-GaAs emission with indirect exciton emission. In n-i-n samples, the spectra do not change significantly upon reversal of V_g polarity.

The crossover between the direct-to-indirect ground state proceeds from the gate voltage behaviour of the direct $\varepsilon_D = E_g - E_D$ and indirect $\varepsilon_I = E_g - E_I - eFd$ exciton energies, where E_g is the band gap including the electron and hole confinement energies in the CQW, E_D and E_I are the direct and indirect exciton binding energies, e is the electron charge, and d is the separation between electron and hole layers. The indirect exciton binding energy is smaller than that for a direct exciton due to the spatial separation of e and h layers, e.g. for GaAs/Al$_{0.33}$Ga$_{0.67}$As CQW with 8 nm QWs and 4 nm barrier (figure 2) $E_I \approx 5\,\text{meV}$ and $E_D \approx 10\,\text{meV}$ [130]. The ε_I shift, equal to eFd, allows the determination of the interlayer separation d, e.g. for the sample shown in figure 2 the shift corresponds to $d = 11.5\,\text{nm}$, which is close to the distance between the QW centres. The direct-to-indirect crossover field, F_{D-I}, is given by $eF_{D-I}d = E_D$–E_I. It is found to increase with magnetic field, see section 2.4. Indirect exciton energy variations with applied electric field are general for various CQW structures: n-i-n AlAs/GaAs CQWs [148, 149, 15], p-i-n InGaAs/GaAs CQWs [17, 125], n-i-n GaAs/AlGaAs CQWs [20, 105, 85]. While the lowest energy exciton states are studied by PL, excited states are studied by the photoluminescence excitation technique, PLE, which is similar to absorption measurements [17, 7, 24].

InGaAs/GaAs CQW samples are characterized by a simple valence band structure due to the large splitting between light- and heavy-hole states. These CQWs allow studying fine features of the direct to indirect transition with applied electric field [17, 44] without additional complications induced by complex valence band structures. Symmetric CQWs (with equal QW widths) can be divided into regimes of narrow barriers and wide barriers with respect to classification of exciton states at $F = 0$. The regime can be parametrized by the ratio of one-particle symmetric to antisymmetric splittings, Δ_{SAS}, and exciton binding energies $\alpha = (\Delta_{\text{SAS}}^{(e)} + \Delta_{\text{SAS}}^{(h)})/(E_D - E_I)$. For CQWs with a wide barrier, $\alpha \ll 1$. In this regime, the exciton states are essentially direct (D) or indirect (I). In order of increasing energy, the exciton states are D symmetric, D antisymmetric, I antisymmetric, and I symmetric. Antisymmetric exciton states are optically inactive, since the oscillator strength, f_{osc}, of the I symmetric exciton is much smaller than that of the D symmetric exciton due to the smaller overlap between the electron and hole. The energy splittings between the D and I excitons are equal to the difference

between the D and I exciton binding energies, $E_D - E_I$. The energy splittings between symmetric and antisymmetric excitons in the wide barrier regime are strongly determined by the Coulomb interaction and are small compared to the one-particle electron/hole Δ_{SAS} splittings [39, 10, 44]. The GaAs/Al$_{0.33}$Ga$_{0.67}$As CQW with 8 nm GaAs QWs and the 4 nm Al$_{0.33}$Ga$_{0.67}$As barrier (figure 2) corresponds to the wide barrier CQWs with $\alpha \ll 1$.

In CQWs with a narrow barrier, $\alpha \gg 1$, the exciton states have a mixed direct–indirect character. In the limit of zero Coulomb interaction, the exciton states can be classified as electron–hole single-particle pair states: S_eS_h, S_eA_h, A_eS_h, A_eA_h, where S and A are symmetric and antisymmetric one-particle electron/hole states. S_eS_h and A_eA_h transitions have equal f_{osc} while S_eA_h, A_eS_h are optically inactive. The energy splitting between the optical transitions is equal to $\Delta_{SAS}^{(e)} + \Delta_{SAS}^{(h)}$. For CQW with arbitrary α the first and the fourth exciton state in order of increasing energy are optically active while the second and the fourth have zero f_{osc}. The ratio of f_{osc} for the first and the fourth exciton states monotonically increases with decreasing α. The In$_{0.2}$Ga$_{0.8}$As/GaAs CQW with 6 nm In$_{0.2}$Ga$_{0.8}$As QWs separated by the 6 nm GaAs barrier (considered in [17, 44]) corresponds to the narrow barrier CQW with $\alpha \gtrsim 1$.

At high electric field, F, the excitons become purely direct or indirect for CQW both with wide and narrow barriers. However, the transition from zero to high electric field regime is obviously different for these two cases [39, 10, 17, 44, 21].

To summarize this section, at low electric fields F (direct regime), the spatially direct exciton is the lowest energy state, while at high F (indirect regime) the indirect exciton composed of an electron and hole in different layers is the lowest energy state. The transition from the direct to indirect regimes is determined by the ratio of the one-particle symmetric–antisymmetric splitting and the exciton binding energies. For a given CQW sample, this ratio and, in turn, the direct-to-indirect crossover can be controlled by magnetic fields [17, 44, 21], see section 2.4. The existence of both direct and indirect regimes in one and the same sample allows verifying an existence of condensation effects for direct and indirect excitons. In all the experiments reviewed below, only the longlife indirect excitons, which are cold, exhibit condensation effects and no condensation effects are observed for the direct excitons, which cannot thermalize down to low temperatures within their short lifetime.

2.2. Repulsive interaction between indirect excitons

An indirect exciton is a dipole oriented perpendicular to the QW plane. The interaction between such dipoles is repulsive. The repulsive interaction between the indirect excitons and, more generally, the monotonic enhancement of energy with increasing density for the system of spatially separated electron and hole layers, stabilizes the exciton state against the formation of metallic electron–hole droplets [144, 146, 99]. Therefore the ground state of the system is excitonic. This is a necessary requirement for the experimental realization of cold exciton gases and ultimately the exciton condensation. Besides, the repulsive interaction results in effective screening of an in-plane disorder potential [68], see section 2.3.

Experimentally, the repulsive interaction is revealed by the enhancement of the exciton energy with increasing density [15, 16, 21, 106, 24]. An example of two different excitation densities is shown in figure 3. Figure 3 shows that, unlike the direct exciton, the indirect exciton energy increases with excitation intensity. This observation is consistent with the theoretically predicted enhancement of the indirect exciton energy with e–h density: it can be understood in terms of the net repulsive interaction between the indirect excitons caused by the dipole–dipole repulsion for low exciton densities, and in terms of the energy shift originating from the electric field between the separated electron and hole layers for high e–h densities.
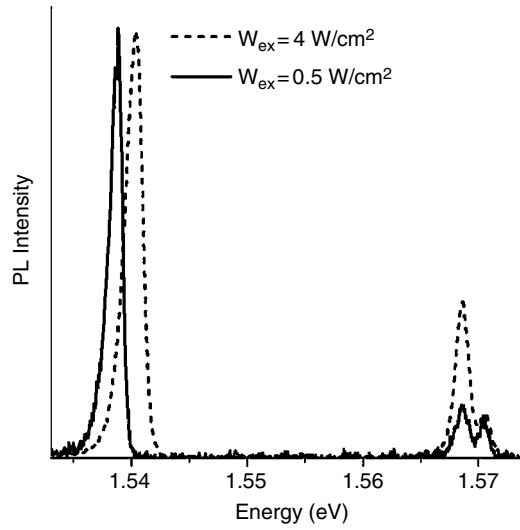
Figure 3. Normalized PL spectra in the indirect regime ($V_g = 1.4\,V$) for $W_{ex} = 0.5$ and $4\,W\,cm^{-2}$ at $T_{bath} = 50\,mK$. From [21].

The strong density dependence of the indirect exciton energy gives a possibility for experimental measurement of the indirect exciton density. The indirect exciton density can be estimated from the energy shift using the plate capacitor formula $\delta E = 4\pi n e^2 d/\varepsilon$, where ε is the dielectric constant. Using the plate capacitor formula results in an underestimation of the exciton density by $\sim$40% for $n = 10^{10}\,cm^{-2}$, a typical exciton density for many experiments [37].

The above consideration of the energy shift is relevant for the case of delocalized excitons for which this shift is determined by exciton–exciton interactions. For the case of localized excitons in a random in-plane potential, the enhancement of the indirect exciton PL energy with increasing density follows (apart from the dipole–dipole repulsion) from the finite degeneracy of the 0D exciton states localized in in-plane potential minima, see section 2.3. The degeneracy can be estimated to be $\sim S/a_B^2$, where S is the exciton localization area. For $N \sim S/a_B^2$ the excitons overlap with each other and their composite structure of two fermions becomes essential [72]. Due to the finite degeneracy, the lower-energy localized exciton states are successively filled with increasing exciton density, which results in enhancement of the mean exciton energy. This implies that the finite degeneracy effects should be dominant at low-exciton densities (and/or low-quality samples with strong in-plane disorder) while for high densities the random potential is screened by the repulsively interacting excitons (section 2.3) and the energy shift should mainly be determined by the interaction effect discussed above. Note however that the system of indirect excitons in CQWs is a system of composite bosons in a random potential. A theory of composite bosons in the presence of interaction and localization is not developed at present. Therefore, the indirect exciton energy shift with increasing density in the presence of a random potential is yet to be understood.

2.3. In-plane disorder

An intrinsic property of any QW system is the in-plane disorder potential which is caused by interface and alloy fluctuations, defects and impurities, and is unavoidable in any QW sample.

High quality samples are characterized by a small amplitude and large length scale of the random potential. This is revealed by a small linewidth of the exciton PL. Conversely, a large in-plane disorder results in a large inhomogeneous broadening of the PL line. Electric-field fluctuations over the CQW plane, $\delta F(x,y)$, create a specific disorder potential for the indirect excitons $\delta E(x,y) \sim \delta F(x,y)ed$. Note also that, compared to the direct excitons, which are neutral entities, the indirect excitons are more sensitive to charge impurities since they are dipoles. The additional disorder for indirect excitons is small in high-quality samples and the indirect exciton linewidth exceeds, only slightly, the direct exciton linewidth, see figure 2. However, strong fluctuations $\delta F(x,y)$ and charged impurities in lower quality samples create a strong additional disorder potential for indirect excitons that should be taken into account.

The random potential strongly influences properties of the exciton condensate in QWs. Note, e.g., that even for infinite 2D systems a disorder results in an in-plane confinement of bosons that allows BEC at nonzero temperatures in analogy to BEC in finite 2D systems, see section 1. The problem of (2D) boson condensation in a disordered medium was studied theoretically [102, 49, 90, 78, 53], mainly in connection with the superfluidity of liquid ^{4}He in porous media or on substrates [120] and superconductivity in granular [143] and uniformly disordered superconductor films [41, 63, 141]. In particular, the boson localization and the superfluid–insulator transition were studied.

A theory of the exciton condensate in a random potential has not been developed so far. The qualitative behaviour of the exciton condensate in an in-plane random potential is supposed to be the following. For moderate potential fluctuations, a random array of the normal areas and exciton condensate lakes (domains) with boundaries determined by the potential profile is formed. The state is analogous to the 'Bose-glass' phase or to a random Josephson-junction array in superconductors. Note that a moderate in-plane random potential improves conditions for the exciton condensation in local potential energy minima because of the confinement effects (T_c increases with reducing confinement area, see section 1) and the enhanced local density driven by the exciton drift towards the bottom of the traps (T_c increases with increasing n, see section 1) [18, 109, 27]. With an increase of the potential fluctuations, the sizes of the condensate lakes (as well as the phase correlation between the lakes) are reduced and at large random potentials the exciton condensate disappears. Note that a very large disorder can result in the breaking of excitons and separate localization of electrons and holes in different potential minima [138]. Therefore, in order to observe the exciton condensate, high quality samples with small potential fluctuations are required. No condensation effects are observed in CQW samples with a large random potential. The disappearance of the effects with increasing disorder is considered, e.g. in [18, 20, 22]. The experiments reviewed in the following sections were performed on the high quality CQW samples characterized by the narrowest PL linewidths.

We note also that the tunnelling time between local potential minima has typically a broad distribution for a given QW (CQW) sample [131]. Therefore, while the energy distribution of the indirect excitons within any potential minimum is thermal (section 1), the equilibration time of the exciton distribution over well-separated potential minima may exceed the lifetime of the indirect excitons and the exciton distribution over these local potential minima would be, therefore, metastable [54, 19, 20].

2.4. Magnetic field effect on indirect excitons

2.4.1. Exciton dispersion measurement and control. This section describes the exciton dispersion control by in-plane and perpendicular magnetic fields as well as the exciton dispersion measurement using in-plane magnetic fields.

The theory of Mott excitons in a magnetic field was first developed by Elliott and Loudon [45, 46] and by Hasegawa and Howard [61] who considered the case of an exciton with zero centre of mass (CoM) momentum. The exciton dispersion relation, i.e., the influence of the exciton motion on its spectrum, was subsequently investigated in the high magnetic field limit (when cyclotron energy is much larger than the Coulomb energy) in the case of 3D excitons [57], 2D excitons in a perpendicular magnetic field [92, 69, 114], and spatially indirect quasi-2D excitons also in a perpendicular magnetic field [100].

In the absence of magnetic field, 2D electrons and holes form a flat hydrogenic bound state. A high magnetic field perpendicular to the xy-plane, $B_\perp$, completely changes this picture, forcing the electron and the hole to travel with the same velocity, $v = \partial E_X/\partial P$, in such a way that they produce on each other a Coulomb force that cancels exactly the Lorentz force [92, 114]. By applying this condition self-consistently, we obtain the 2D-magnetoexciton dispersion relation, $E_X = E_X(P)$, and, in turn, its binding energy E_B and effective mass M_B. In the high magnetic field limit, the problem can be solved analytically [92].

In the following, we use the notations for the magnetic length $l_B = [\hbar c/(eB_\perp)]^{1/2}$, the cyclotron energy $\hbar\omega_c = \hbar eB_\perp/(\mu c)$, the 3D-exciton Bohr radius $a_B = \varepsilon\hbar^2/(\mu e^2)$ and its binding energy $R_y = \mu e^4/(2\varepsilon^2\hbar^2)$, here m_e, m_h and $\mu = m_e m_h/(m_e+m_h)$ are respectively the effective masses of e and h and the e–h reduced mass, and we measure the exciton energy from the semiconductor gap.

In the high magnetic field limit, one can demonstrate analytically the following results for 2D-magnetoexcitons built up from e and h in the 0th Landau levels (LLs) [92]: (i) the magnetoexciton binding energy is proportional to the square root of $B_\perp$, $E_B = (\pi/2)^{1/2}e^2/(\varepsilon l_B) \sim (B_\perp)^{1/2}$, (ii) the magnetoexciton dispersion relation is given by $E_X(P) = -E_B e^{-\beta}I_0(\beta)$, where $I_0(x)$ is the modified Bessel function, $\beta = [Pl_B/(2\hbar)]^2$, (iii) for small momenta $Pl_B/\hbar \ll 1$, the magnetoexciton dispersion is parabolic and is characterized by an effective magnetoexciton mass $M_B = (2^{3/2}\varepsilon\,\hbar^2)/(\pi^{1/2}e^2 l_B) \sim (B_\perp)^{1/2}$, (iv) for a magnetoexciton with $P = 0$ the magnetic length plays the role of the Bohr radius, (v) magnetoexcitons with momentum $\mathbf{P}$ carry an electric dipole in a direction perpendicular to $\mathbf{P}$ whose magnitude, $e\langle\mathbf{r}\rangle = e\langle\mathbf{r}_e - \mathbf{r}_h\rangle = e\hat{\mathbf{z}} \times \mathbf{P}l_B^2/\hbar$, is proportional to P. This expression makes explicit the coupling between the centre-of-mass (CoM) motion and the internal structure. The coupling results in a curious property, called the electrostatic analogy: the dispersion $E_X(\mathbf{P})$ can be calculated from the expression of the Coulomb force between e and h as a function of $\langle\mathbf{r}\rangle$ and has the unusual consequence that the magnetoexciton mass and binding energy depend on $B_\perp$ only and are independent of m_e and m_h. Contrary to the e–h system at zero magnetic field (hydrogenic problem), all e–h pairs are bound states and there is no scattering state. At $Pl_B/\hbar \gg 1$, the separation between e and h tends to infinity and the magnetoexciton energy tends towards the sum of the lowest e and h Landau level energies, i.e. $\frac{1}{2}\hbar\omega_c = \frac{1}{2}\hbar eB_\perp/(\mu c)$.

The internal structure and dispersion relation of the 2D-magnetoexciton are qualitatively different from those of the 2D-exciton at zero magnetic field. This is clearly seen by comparing the lowest energy states which evolve into each other when B is varied: the magnetoexciton builds up from e and h in the 0th LLs and the 1S-exciton, for which $E_X(P) = P^2/2M_X - E_b$ and $\langle\mathbf{r}\rangle = 0\ \forall P$, $M_X = m_e + m_h$ is the exciton mass and $E_b = 4R_y$ is the 2D-exciton binding energy.

The transition from the 2D-exciton at zero magnetic field to the 2D-magnetoexciton is nontrivial. It was studied by Lozovik *et al* both for direct excitons in single QWs and indirect excitons in CQWs in [101]. For weak $B_\perp$ and small momenta P, the e–h Coulomb attraction is dominant and the exciton structure is that of a strongly bound hydrogenic e–h state slightly modified by $B_\perp$. In the other regime, at high $B_\perp$ or large P, the exciton structure is dominated by the interaction of each carrier with the magnetic field. The later regime occurs for large values

of P even at weak $B_\perp$ when the e–h separation in the xy-plane is large, $\langle \mathbf{r} \rangle = z \times \mathbf{P}l_B^2/\hbar$, and the Coulomb interaction is small compared to the interaction with the magnetic field. The excitons in these regimes were called 'hydrogen-like excitons' and 'magnetoexcitons', respectively [101]. For magnetic fields smaller than a critical value B_0 there is a sharp transition between these two regimes as P grows. At the transition, the e–h separation in the ground state abruptly increases to $\langle \mathbf{r} \rangle = \rho_0 = cP/(eB_\perp)$, i.e. suddenly the size of the exciton blows up, and the exciton dispersion relation abruptly changes from a quadratic dependence, $E_X(P) \sim P^2$ for $P < P_{tr}(B_\perp)$, to being practically independent of P, $E_X(P) \approx \frac{1}{2}\hbar\omega_c$ for $P > P_{tr}(B_\perp)$. In the high magnetic field regime, defined by E_b, $E_B \ll \hbar\omega_c$, only the magnetoexciton regime exists and $\langle \mathbf{r} \rangle = cP/(eB_\perp)$, $\forall P$, whereas for intermediate fields the transition smears out into a crossover region. The 'phase diagram' for the 'hydrogen-like excitons' and 'magnetoexcitons' on the plane *magnetic field versus exciton momentum* was studied in [101].

The basic features of the indirect magnetoexciton are the same as that of the direct magnetoexciton. However, because of the separation between the electron and hole layers the indirect magnetoexciton binding energy and effective mass differ quantitatively from those of direct magnetoexcitons. As the interlayer separation d increases, the indirect magnetoexciton binding energy reduces whereas its effective mass increases. In particular, in the high magnetic field limit $M_{Bd} = M_B[1 + 2^{3/2}d/(\pi^{1/2}l_B)]$ for $d \ll l_B$, and $M_{Bd} = M_B\pi^{1/2}d^3/(2^{3/2}l_B^3)$ for $d \gg l_B$ [100]. The effective mass enhancement is easily explained using the electrostatic analogy: for separated layers, the e–h Coulomb interaction is weaker than that within a single layer and changes only slightly for $\langle r \rangle < d$; this implies that $E_X(P)$ increases only slowly for $P < \hbar d/l_B^2$; in other words, the indirect magnetoexcitons have a large effective mass. Measurements of the indirect (magneto)exciton dispersion and effective mass are reviewed at the end of this subsection.

In the following two paragraphs, we discuss briefly the effects of perpendicular magnetic fields on the direct-to-indirect exciton transition and on the PL energy. The direct-to-indirect crossover field, $F_{D-I} = (E_D - E_I)/(ed)$ (see section 2.1), is found to increase with magnetic field (figure 2). This corresponds to the stronger enhancement with magnetic field of the direct exciton binding energy, E_D, compared to E_I [17, 44, 21]. Particularly, in the high magnetic field limit, these energies are evaluated as $E_D \sim 1/l_B$ and $E_I \sim 1/(l_B^2 + d^2)^{1/2}$. The magnetic field dependence of the indirect exciton binding energy, direct-to-indirect crossover, and diamagnetic shift in finite magnetic fields were calculated in [44], in particular for the sample studied in [17]; the calculations are in quantitative agreement with the experimental data. Besides the ground state, an indirect exciton composed from an electron and a hole on zero Landau levels, the experiment [17] and the theory [44] addressed also excitons composed from electrons and holes on higher Landau levels. The later states were studied experimentally using PLE techniques [17].

The magnetic field dependence of the PL spectrum in the indirect regime is presented in figure 4. The indirect line $\varepsilon_I = E_g + \hbar\omega_c/2 - E_I - eFd$ shifts with $B_\perp$ to higher energies stronger than the direct line $\varepsilon_D = E_g + \hbar\omega_c/2 - E_D$, which reflects again the stronger enhancement of E_D with magnetic field. Monotonic enhancement of the indirect exciton PL energy with $B_\perp$, the diamagnetic shift, was observed in [17, 21, 86]. The shift measured in [17] is in quantitative agreement with the theory of indirect excitons in magnetic fields [44] which was applied to the indirect excitons with parameters of those of [17]. In contrast, a reduction of PL energy with increasing $B_\perp$ was observed in [79, 107]. This reduction is inconsistent with the theory of indirect magnetoexcitons and most likely originates from magnetic-field-induced variations of the applied electric field, F, which take place due to the imperfectness of the insulating and metallic layers in the CQW samples studied in [79, 107], see section 2.1. Magnetic-field-induced variations of F were discussed in [79].
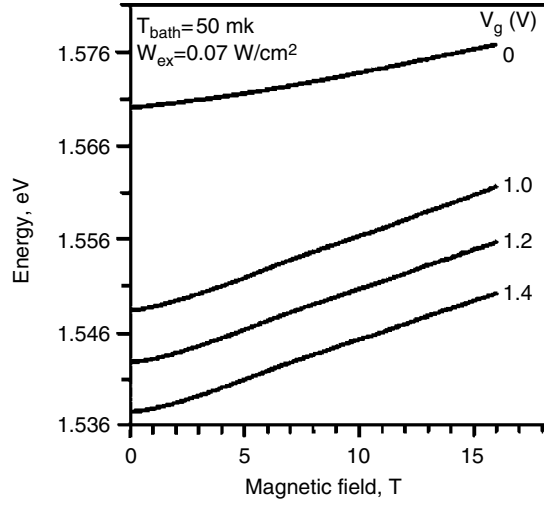
Figure 4. Magnetic field dependences of the direct (at $V_g = 0$) and indirect (at $V_g = 1$, 1.2, and 1.4 V) exciton PL line position for different gate voltages, V_g. From [21].

We now discuss exciton dispersion measurement and control by the in-plane magnetic field. Due to the coupling between the internal structure of magnetoexciton and its centre-of-mass motion [57] the ground exciton state in a direct-band-gap semiconductor in crossed electric and magnetic fields was predicted to be at a finite momentum. In particular, the transition from the momentum-space direct exciton ground state to the momentum-space indirect exciton ground state was predicted (1) for spatially indirect, inter-well, excitons in CQW in an in-plane magnetic field [97, 56], and (2) for single layer excitons in an in-plane electric field and perpendicular magnetic field [42, 114, 65]. In this subsection we consider the effect of the in-plane magnetic field on spatially indirect excitons in CQW.

In-plane magnetic field $B_\parallel$ has no effect on spatially direct excitons, whereas for spatially indirect excitons it shifts the dispersion curve by $e\,dB_\parallel/c$ without changing its shape (to the second order in $B_\parallel$ and the QW width) in the in-plane direction perpendicular to $B_\parallel$ [56, 23, 115, 26] as illustrated in figure 5. The shift allows (1) experimental measurements of the exciton dispersion and, in particular, the exciton mass and (2) controllable variation of the exciton dispersion $E_X(P)$ and an increase of the lifetime for the exciton ground state.

It is well known that only the free exciton states that can recombine radiatively are those inside the intersection between the dispersion surface $E_X(P)$ and the photon cone $E_{ph} = Pc/\varepsilon^{1/2}$, called the radiative zone [47, 60, 4, 38, 34, 8] (ε is the background dielectric constant). In GaAs structures the radiative zone corresponds to small CoM momenta $P/\hbar \lesssim K_0 \approx E_g\varepsilon^{1/2}/(\hbar c) \approx 2.7 \times 10^5\,\mathrm{cm}^{-1}$. Therefore, as $B_\parallel$ increases, the intersection of the photon cone with the exciton dispersion surface varies and the energy of the excitons that are coupled to light, following the intersection, tracks the dispersion surface (figure 5). Thus by measuring the magnetoexciton photoluminescence (PL) energy as a function of the in-plane magnetic field $B_\parallel$ one can determine the dispersion of the spatially indirect exciton.

For the GaAs/AlGaAs CQW with $d \approx 11.5\,\mathrm{nm}$ studied in [23, 26] the shift induced by strong in-plane magnetic fields $K_B = e\,dB_\parallel/(\hbar c)$ is much larger than K_0. For example, at $B_\parallel = 12\,\mathrm{T}$, $K_B \approx 2.1 \times 10^6\,\mathrm{cm}^{-1} \sim 8K_0$. Furthermore, for the narrow QWs the diamagnetic shift of the bottom of the bands is very small and can be neglected [128], as confirmed by the negligible variation in the spatially direct transitions in the experiments of [23, 26]. Therefore,
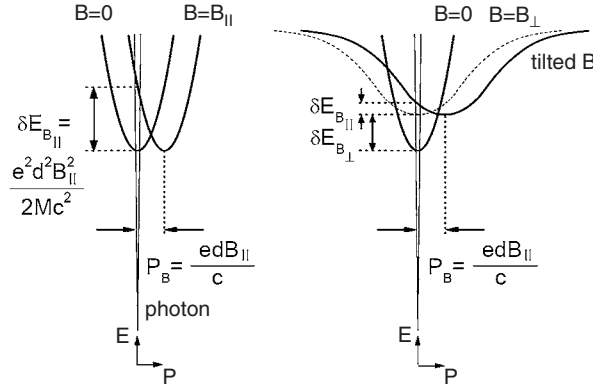
Figure 5. Schematic of the indirect exciton dispersion at zero B and in-plane B (left) and at zero B, perpendicular B, and tilted B (right). The optically active exciton states are within the radiative zone determined by the photon cone.

the peak energy of the indirect exciton PL is set by the energy of the radiative zone and is given as a function of $B_\parallel$ by $E_{P=0} = P_B^2/(2M_X) = e^2d^2B_\parallel^2/(2M_Xc^2)$ for a parabolic dispersion, i.e., it is inversely proportional to the indirect (magneto)exciton mass M_X (figure 5). In general, the method for exciton dispersion measurement is good for CQWs with a large interlayer separation d and narrow QWs.

Using the shift in the indirect exciton PL line versus $B_\parallel$, the (magneto)exciton dispersions were measured for various $B_\perp$ in [26], figure 6(a). In turn, the (magneto)exciton effective mass at the band bottom was determined by quadratic fits to the dispersion curves at small P. At $B_\perp = 0$, the PL energy shift rate corresponds to $M_X = 0.22m_0$ in good agreement with the calculated mass of a heavy hole exciton in GaAs QWs $\approx 0.25m_0$ ($m_e = 0.067m_0$ and an in-plane heavy hole mass $m_h = 0.18m_0$ [3, 6, 118]). We note that the method allows a proper measurement of the exciton dispersion and effective mass only if the exciton momentum is well determined. This requires high-quality samples with a large mean free path of the exciton l: the exciton momentum uncertainty $\hbar/l$ should be smaller than $\hbar K_0 \approx E_g\varepsilon^{1/2}/c$. The higher value of the exciton mass, $\sim 0.5m_0$, measured using the method in [115] results probably from the high in-plane disorder in the samples studied in [115] as revealed by the large PL linewidth, ~ 5 meV.

Drastic changes in the magnetoexciton dispersion are observed at finite $B_\perp$. The dispersion curves become significantly flat at small momenta as seen in figure 6. This corresponds to a strong enhancement of the magnetoexciton mass: already at $B_\perp = 4$ T the magnetoexciton mass has increased by about three times and at higher $B_\perp$ the dispersions become so flat that the scattering of the experimental points does not allow precise determination of the mass which becomes very large.

The calculated effective mass enhancement is in agreement with the experimental data (there was no fitting parameter in the calculations that used measured $M_X = 0.22m_0$ at $B_\perp = 0$ and $d = 11.5$ nm), e.g. at $B_\perp = 4$ T the measured magnetoexciton mass increase is 2.7 as compared to the theoretical value 2.5, see figure 6. Note, however, that the quantitative difference between experiment and theory for the rate of energy increase with momentum at the largest magnetoexciton momenta is unclear.

As mentioned above, the shift of the exciton dispersion curve by $e\,dB_\parallel/c$ in the in-plane magnetic field $B_\parallel$ allows controllable variation of the exciton dispersion $E_X(P)$ and an increase
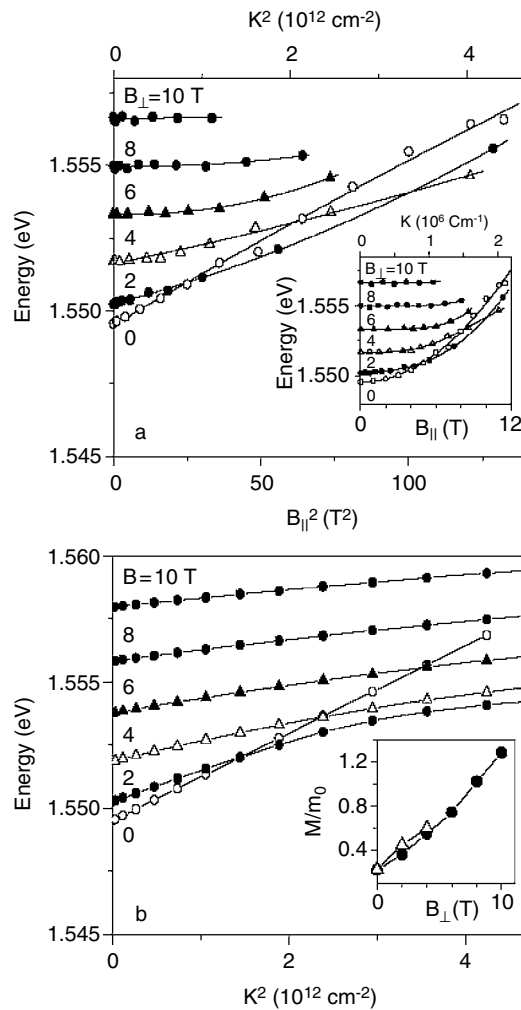
Figure 6. (a) Measured and (b) calculated magnetoexciton dispersions at $B_\perp = 0$, 2, 4, 6, 8, and 10 T versus K^2. Upper inset: measured magnetoexciton dispersions versus K ($B_\parallel$). Lower inset: measured (triangles) and calculated (circles) magnetoexciton mass at the band bottom versus $B_\perp$. From [26].

of the lifetime for the exciton ground state. Experimentally, a strong enhancement of the indirect exciton lifetime was observed in in-plane magnetic fields, by more than 20 times in $B_\parallel = 12$ T, in [23]. This reflects the displacement of the indirect exciton dispersion and, in turn, the nonradiative character of the ground exciton state—in in-plane magnetic fields the spatially indirect excitons become both space- and momentum-indirect. The nonradiative character of the ground state of an indirect exciton in in-plane magnetic fields is revealed also by the temperature dependence of the PL kinetics. At zero magnetic field, the exciton recombination rate monotonically reduces with increasing temperature due to the thermal reduction of the radiative zone occupation [20, 23]. In high in-plane magnetic fields, the temperature dependence is the opposite: the exciton recombination rate increases with increasing temperature due to the increasing occupation of the radiative zone [23]. An in-plane

magnetic field is a tool for exciton dispersion engineering and the controllable increase of the exciton ground-state lifetime.

To summarize, this subsection described exciton dispersion control by in-plane and perpendicular magnetic fields as well as exciton dispersion measurement by in-plane magnetic fields. The perpendicular magnetic fields result in a diamagnetic shift of the exciton, change the shape of the exciton dispersion, and change the exciton binding energy and effective mass, while in-plane magnetic fields shift the dispersion curve of the indirect exciton by $e\,dB_\parallel/c$ without changing its shape (to the second order in $B_\parallel$ and the QW width).

2.4.2. Effect of perpendicular magnetic field on exciton condensation. The observed large increase of the effective mass of the indirect exciton in magnetic fields is a single-exciton effect, in contrast to the well-known renormalization effects in neutral and charged e–h plasmas [121, 12, 13, 14]. It has, however, very important effects on collective phenomena in the exciton system. In particular, the mass enhancement explains the disappearance of the stimulated exciton scattering and the transition from a highly degenerate to a classical exciton gas with increasing magnetic field observed in [25].

In general, the magnetic field effect on the quantum degeneracy of the 2D exciton gas and the exciton condensation to the $P=0$ state has a complicated character [101]. There are the 'good' effects induced by the magnetic field which increase the quantum degeneracy and improve the critical conditions for the exciton condensation, and there are the 'bad' effects which, conversely, reduce the quantum degeneracy and suppress the exciton condensation.

The 'good' effects of applying a magnetic field are: (g1) it lifts off the spin degeneracy, g, resulting in an increase of the quantum degeneracy and of the exciton condensation critical temperature T_c which are both $\propto 1/g$ (section 1). (g2) It increases the exciton binding energy, reduces the ground state radius, and reduces screening. This increases the exciton stability and maximizes the exciton density which can be reached (limited by the Mott transition, which is determined by phase-space filling and screening, and inversely proportional to the square of the exciton radius [121]) and therefore increases the quantum degeneracy and T_c for high exciton densities. (g3) It results in the coupling between the exciton CoM motion and internal structure. This coupling modifies the nature of the exciton condensation: at $B=0$ the exciton condensation is purely determined by the statistical distribution in momentum-space of weakly interacting bosons (i.e. excitons) [72], while in the high magnetic field regime, due to the coupling, the e–h Coulomb attraction forces the excitons to the low-P states, and, therefore, the mean field critical temperature T_c at which the quasi-condensate appears [116, 9, 48] in the high magnetic field limit is determined (within the mean field approximation valid at not very low LL filling factors) by the e–h pairing [91, 83, 93, 94] similar to the case of the excitonic insulator [71] or Cooper pairs. According to the theory of [91, 83, 93, 94], T_c in high magnetic fields is much higher than T_c at $B=0$ (see for example figure 1 in [18]).

The 'bad' effects of applying a magnetic field are: (b1) According to [144, 33], in high magnetic fields the exciton condensate can be in the ground state only if the separation between the layers is small $d < l_B$. For large d or small l_B the e–e and h–h rather than the e–h correlations determine the ground state of spatially separated e and h layers. Therefore, magnetic fields such that $l_B < d$ should destroy the condensate. (b2) According to the previous section, the magnetic field increases the in-plane exciton mass M_X and, therefore, reduces the quantum degeneracy of the 2D exciton gas and T_c which are both $\propto 1/M_X$ (section 1). (Note that the Kosterlitz–Thouless transition temperature is also $\propto 1/M_X$ [77, 48].)

Some of the 'good' and the 'bad' effects are crucially dependent on the interlayer separation d. In particular, small d is essential to maximize the (g2) and (g3) effects as the binding energy
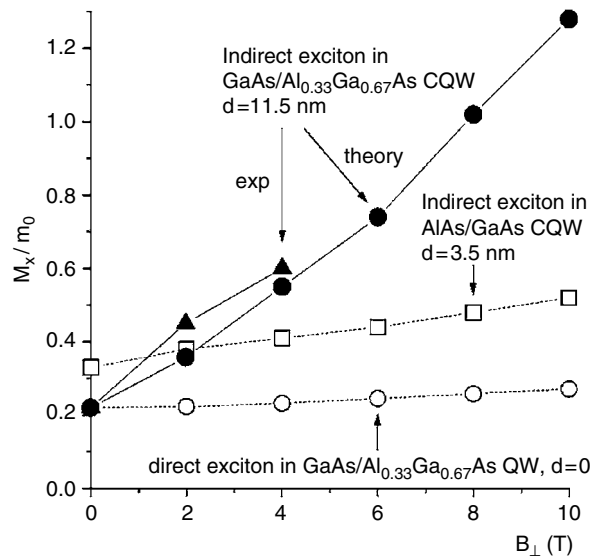
Figure 7. Calculated effective masses of indirect (points) and direct (circles) excitons in GaAs/Al$_{0.33}$Ga$_{0.67}$As CQW with $d = 11.5$ nm versus $B_\perp$. Triangles correspond to the experimental data for indirect excitons in GaAs/Al$_{0.33}$Ga$_{0.67}$As CQW with $d = 11.5$ nm. Squares correspond to the calculated effective mass of an indirect exciton in AlAs/GaAs CQW with $d = 3.5$ nm. From [101].

of indirect excitons is higher for smaller d. Small d is also essential to overcome the (b1) effect, namely, for smaller d it is possible to reach higher magnetic fields before $l_B \sim d$. The results shown in figure 7 present probably the most important difference in the magnetic field effect on the quantum degeneracy of the exciton gas and on the exciton condensation for the systems with small and large d: for large d, the magnetic field results in a huge enhancement of M_X, while for small d the mass enhancement is not significant. Therefore, a magnetic field could increase the quantum degeneracy of a 2D exciton gas and improve the critical conditions for the exciton condensation in systems of spatially separated electron and hole layers with small d and, vice versa, reduce the quantum degeneracy of the 2D exciton gas and suppress the exciton condensation in systems of spatially separated electron and hole layers with large d. These results could explain the opposite effect of the magnetic field on the indirect excitons in AlAs/GaAs CQWs with $d = 3.5$ nm, where magnetic field improves the critical conditions for the exciton condensation [15, 16, 18], and on the indirect excitons in GaAs/Al$_{0.33}$Ga$_{0.67}$As CQWs with $d = 11.5$ nm, where magnetic field reduces the quantum degeneracy of the 2D gas of indirect excitons [25], see section 3.

3. Experimental studies of cold exciton gases and exciton condensation

### 3.1. Anomalous transport and luminescence of indirect excitons in AlAs/GaAs CQWs

As discussed in the previous section, magnetic fields improve the critical conditions for the exciton condensation for systems with a small separation between electron and hole layers, d, while for the systems with a large d, the magnetic field effect is dominated by the exciton mass enhancement that reduces the quantum degeneracy of 2D exciton gas and T_c which are

both $\propto 1/M_X$ [101]. Experimental studies of 2D exciton gas with a small separation between electron and hole layers were performed using AlAs/GaAs CQWs where d is about 3.5 nm (figure 1(b)).

Condensation of longlife interacting indirect excitons in CQWs should be accompanied by the appearance of exciton superfluidity [97]. The interaction results in the linear dispersion of the collective modes in the exciton system and, consequently, in fulfillment of the Landau criterion of superfluidity [97, 83, 94, 114], while the problem of the order parameter phase fixation [76, 59] is removed due to the long lifetime of indirect excitons [97, 98]. The latter problem was pointed out by Kohn and Sherrington [76] and by Guseinov and Keldysh [59] and is the following: the interband transitions (e–h recombination for semiconductor systems and tunnelling for semimetal systems) fix the phase of the exciton condensate order parameter which makes impossible the superfluid state with uniform particle flow. The highest interband transition rate at which the exciton superfluidity is still possible was calculated in [98].

For measurements of exciton transport, a time-of-flight technique has been used: the PL decay from an unmasked part of the sample was compared with the PL decay from a part of the sample which was covered by a nontransparent NiCr mask, leaving an array of 4 μm wide stripes uncovered and separated from each other by 32 μm [18]. The PL decay for the masked part of the sample is more rapid compared to that for the unmasked part due to the exciton transport out of the window regions that allows direct measurements of exciton transport characteristics. In addition, the measurements of the exciton transport in AlAs/GaAs CQWs performed simultaneously with the PL decay measurements have shown that the exciton nonradiative decay rate τ_{nr}^{-1} ($\tau_{nr}^{-1} \approx \tau^{-1}$, the exciton decay rate for the studied AlAs/GaAs CQWs with low quantum efficiency) is mainly determined by exciton transport to nonradiative recombination centres and is increased with increasing exciton mobility [18]. Therefore, for the samples studied in [18], the faster PL decay corresponds to more rapid exciton transport. A strong enhancement of the exciton mobility was observed at the expected conditions for the exciton condensation, i.e. at low temperatures and high magnetic fields (figures 8(b) and (d)). No explanation for this effect in terms of single exciton transport has been found so far. A possible explanation for this effect, the validity of which is argued in [18], is the onset of exciton superfluidity. In contrast, the increase of the exciton mobility with temperature and its reduction with magnetic field observed at high temperatures and/or low magnetic fields in [18] are typical for thermally activated single exciton transport in a random potential [55, 43].

Besides the exciton superfluidity, another signature of the exciton condensation is the onset of exciton superradiance (macroscopic dipole), which can be detected as an increase of the exciton radiative decay rate [18, 109]. This effect originates from an enhancement of the exciton coherent area at the exciton condensation. In the general case, the oscillator strength of the optically active 2D excitons is increased with the increase in the lateral size of the exciton centre-of-mass wave function, called the exciton coherent area, and saturates when the coherence length reaches the inverse wave vector of the emitted light [47, 60, 4, 38, 34, 8]. For normal uncondensed excitons the coherent length is determined by the exciton localization length and the exciton scattering length [47, 60, 4, 38, 34, 8]. For the condensed excitons the whole size of the condensate is the coherent area which implies large exciton oscillator strength. The mechanism for the increase of the exciton coherence area at the exciton condensation in the presence of the random potential is nontrivial and requires theoretical consideration. It follows presumably from the increase of the exciton–exciton and exciton–phonon scattering length at the exciton condensation as well as from the increase of the exciton localization length due to the enhanced exciton screening of the random potential at the condensation [109] and due to the settling of the phase coherence among the condensate lakes (the latter effect was briefly discussed in [90]).
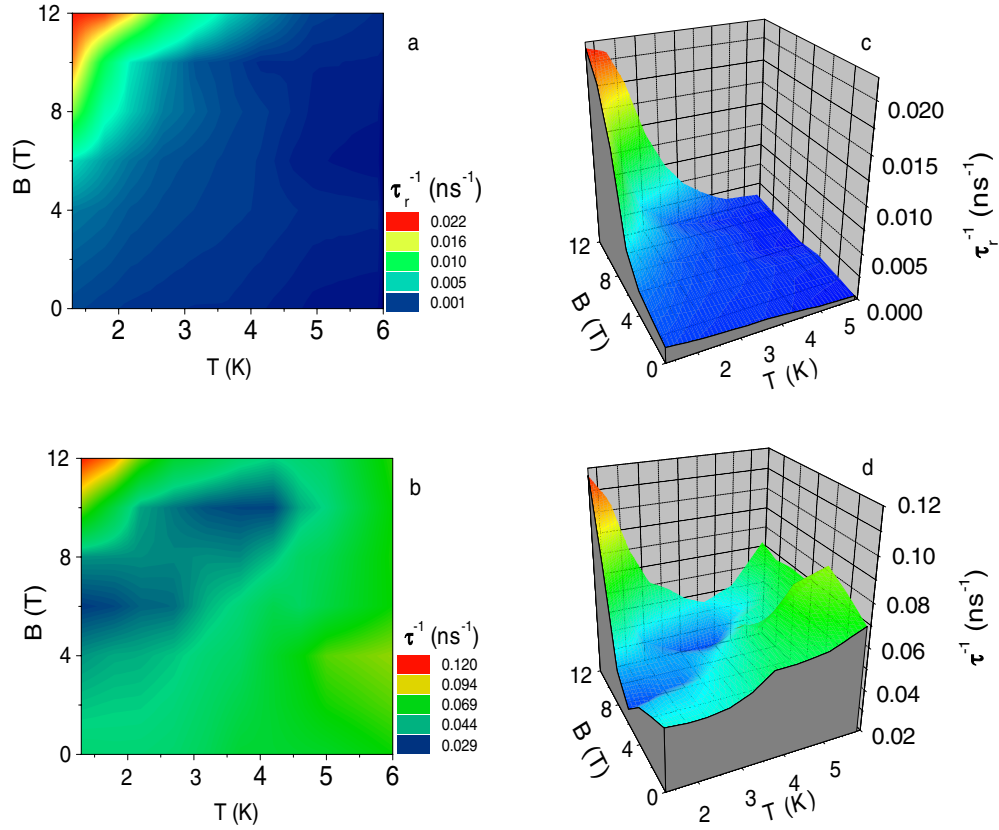
Figure 8. Temperature and magnetic field dependences of the radiative decay rate τ_r^{-1} (a, c) and the initial decay rate τ^{-1} (b, d) of the indirect excitons in AlAs/GaAs CQW. The variations of τ^{-1} reflect the changes in exciton transport with the larger τ^{-1} corresponding to the faster exciton transport, see text. From [18, 29].

The increase of the exciton radiative decay rate at the exciton condensation refers to the excitons that are direct in x–y momentum space. The indirect excitons in the AlAs/GaAs CQWs studied in [15, 16, 18,19] are of X_z type, i.e. they are direct in x–y momentum space. The exciton radiative decay rate τ_r^{-1} can be directly derived from the measured τ and the time-integrated exciton PL intensity I_{PL}. In the case of monoexponential PL decay $\tau_r^{-1} \approx (I_{PL}/I_D)\tau^{-1}$, where I_D is the integrated PL intensity in the direct regime measured at the same excitation (see [18] for details). A strong and sharp increase of τ_r^{-1} with reducing temperature and increasing magnetic field was observed [18]: the variation of τ_r^{-1} increases by about 60 times when going from the lower right corner to the upper left corner of the diagram plane (figures 8(a) and (c)). This indicates a strong and sharp increase of the exciton coherence area. No explanation for this effect in terms of the emission of normal uncondensed excitons was found so far. Because the strong and sharp increase of τ_r^{-1} is observed at the expected conditions for the exciton condensation, i.e. at low temperatures and high magnetic fields, and because this increase is expected for the exciton condensation, the observed huge increase of τ_r^{-1} most likely corresponds to the exciton condensate superradiance, i.e. formation of a macroscopic dipole, as argued in [18]. In contrast, the small increase of τ_r^{-1} observed with increasing magnetic field at high temperatures, $> 5\,\mathrm{K}$, corresponds to the shrinkage of the in-plane relative e–h wave
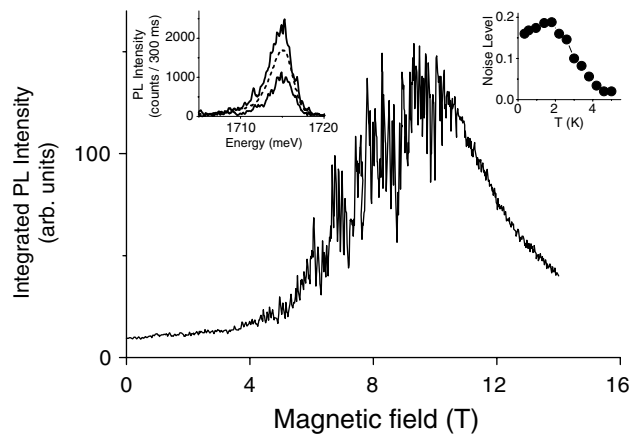
Figure 9. Magnetic field dependence of the integrated PL intensity of the indirect excitons in AlAs/GaAs CQW at cw excitation at $T = 350$ mK. Right inset: temperature dependence of the noise level $<\delta I_{PL}> / <I_{PL}>$ at $B = 9$ T. Left inset: long-time integrated indirect exciton PL spectrum (dashed line) and indirect exciton PL spectra integrated during 0.3 s (solid lines) in the noise regime. From [18, 29].

function, while the small increase of τ_r^{-1} observed with reducing temperature at low magnetic fields, $B < 4$ T, corresponds to the gradual increase of $P < P_0$ state filling (see section 2.4.1) and of the coherent area for normal uncondensed excitons [18]. While for normal uncondensed excitons, reducing the temperature results in a gradual and small increase of the coherent area, the exciton condensation is characterized by a strong and sharp increase of the exciton coherent area at the critical temperature.

The anomalous rapid exciton transport and large τ_r^{-1} are observed in approximately the same range of parameters—at low temperatures and high magnetic fields (figure 8). They are strongly reduced with reducing excitation density W (while at low magnetic fields and high temperatures the exciton transport and τ_r^{-1} only weakly depend on W) [18]. This qualitatively corresponds to the expected disappearance of the exciton superfluidity and superradiance for the exciton condensate with reducing exciton density in a random potential as discussed in [18].

Observation of a substantial increase of the radiative decay rate of indirect excitons in CQWs at low temperatures was also reported and interpreted in terms of the collective behaviour of the indirect excitons and the exciton condensation in [85–88].

A spectacular effect has been observed under cw photoexcitation in high magnetic fields, namely, a huge broad-band noise in the integrated PL intensity of indirect excitons [15, 16] (figure 9). The average variation of the integrated PL intensity is connected with variations of the radiative and nonradiative decay times of indirect excitons discussed above. The power spectrum of the anomalously large noise has a broadband spectrum. The noise is observed at low temperatures (figure 9). The spectral position of the PL line is practically constant during the intensity fluctuations (figure 9), which shows that the noise cannot be related to fluctuations of the CQW potential profile in the z direction (including fluctuations in the applied electric field F).

The appearance of noise is often treated as evidence for the presence of coherence in a system: in a variety of experiments, the noise amplitude is known to be inversely proportional to the number of statistically independent entities in a system and large noise amplitudes therefore

denote that only a small number of entities exist in the macroscopically large system [2]. In particular, in counting experiments with a count rate N, the noise level is $\delta N/\langle N \rangle \sim 1/\sqrt{N}$. For the considered experiment with the number of excitons in the system of the order of 10^6 and the count rate of the detected photons over the detector averaging time exceeding 10^4, the noise level should not exceed 1% for the case of independently fluctuating light emitters—the excitons. A higher noise level implies that the photon emissions by different excitons are correlated, that leads to a reduction of the number of independent entities N and, in turn, to an increase of the noise level. The observed large noise by itself does not specify the origin of the correlation of the photon emissions by different excitons, i.e. the origin of the formation of macroscopic emitting entities in the exciton system. Since the noise is observed at low temperatures (figure 9) the macroscopic emitting entities are formed at low temperatures. The appearance of macroscopic emitting entities in the exciton system is consistent with the exciton condensation. A condensed lake can be considered as one macroscopic entity. Due to the high radiative decay rate of the exciton condensate, the PL signal of condensed excitons is much higher as compared to uncondensed ones. Therefore, formations and disappearances of condensate lakes would result in fluctuations of the total PL signal. Note that within this model large fluctuations of the total PL signal are possible because of the small PL quantum efficiency of normal uncondensed indirect excitons, which can be strongly increased in the condensate lake sites at the exciton condensation. The noise is observed only on the left slope of the $I_{PL}(B)$ dependence (figure 9), i.e. the noise appears in the range of magnetic fields where τ_r^{-1} starts to increase, and disappears in the range of magnetic fields where τ_r^{-1} saturates and rapid exciton transport is observed. Therefore, the noise could be related to fluctuations near the phase transition connected with an instability of the condensate lakes [18].

Note that another type of fluctuation of the indirect exciton PL signal at a given PL energy can result from fluctuations of the CQW potential profile in the z direction and in particular fluctuations of the applied electric field F due to the corresponding fluctuations of the indirect exciton PL energy $\delta E = e\, d\delta F$. Fluctuations of this type were observed in [108]. They are clearly distinguished by the accompanying fluctuations of the indirect exciton energies. The fluctuations in F can be avoided by the proper design of the insulating and metallic layers in the CQW samples, see above. Fluctuations of the indirect exciton PL signal were reported also in [139, 79, 80].

3.2. Stimulation kinetics of excitons

The scattering rate of bosons to a state $\mathbf{p}$ is proportional to $(1 + N_{\mathbf{p}})$, where $N_{\mathbf{p}}$ is the occupation number of the state $\mathbf{p}$. At high $N_{\mathbf{p}}$ the scattering process is stimulated by the presence of other identical bosons in the final state. The stimulated scattering is a signature of quantum degeneracy. It is considered to be a spectacular signature for BEC in atomic gases [75].

In this and the following sections, we briefly review experiments on excitons in high quality GaAs/Al$_x$Ga$_{1-x}$As CQWs (figure 1(a)) where radiative recombination is dominant. The PL kinetics of indirect excitons are shown in figure 10(a) [25]. At low excitation, after a rectangular excitation pulse is switched off, the PL intensity of indirect excitons decays nearly monoexponentially. In contrast, at high excitation, right after the excitation pulse is switched off the PL intensity jumps up and starts to decay only in a few nanoseconds. As discussed above, for delocalized, in-plane, free quasi-2D excitons, only the states with small centre-of-mass momenta $|\mathbf{P}| \leqslant P_0 \approx E_g \varepsilon^{1/2}/c$ can decay radiatively by resonant emission of bulk photons [47, 60, 4, 38, 34, 8] (see figure 11(a)). Thus the PL dynamics is determined by the occupation kinetics of the optically active low-energy states $E \leqslant E_{p0}$, the radiative zone ($E_{p0}/k_B = p_0^2/2Mk_B \approx 1.2$ K at $B = 0$). The LA-phonon-assisted relaxation of the optically
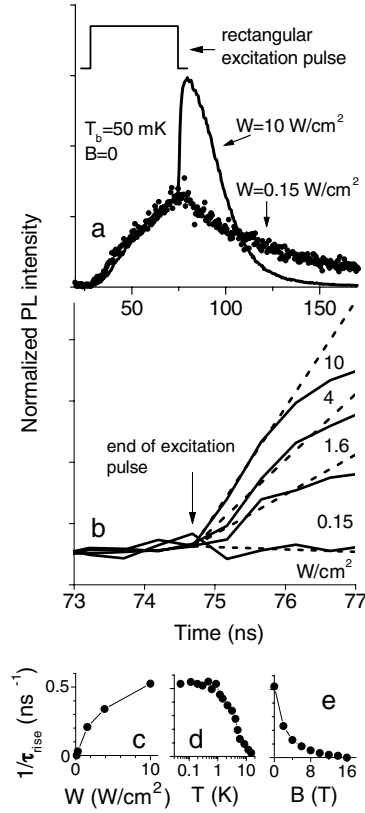
Figure 10. (a) PL kinetics of indirect excitons in GaAs/AlGaAs CQW at high and low excitation W. (b) PL kinetics of indirect excitons near the end of the excitation pulse at different W. The rate $1/\tau_{\text{rise}}$ of the PL rise after the end of the excitation pulse is presented in (c), (d) and (e) versus W at $T_{\text{b}} = 50$ mK and $B = 0$, bath temperature T_{b} at $W = 10$ W cm^{-2} and $B = 0$, and magnetic field B at $W = 10$ W cm^{-2} and $T_{\text{b}} = 50$ mK, respectively. From [25, 29].

dark hot photoexcited indirect excitons into the optically active low-energy states results in a rise of the PL signal, while optical recombination of the low-energy indirect excitons results in a decay of the PL intensity. The end of the excitation pulse is accompanied by a sharp drop in the exciton temperature, caused by switching off the generation of hot indirect excitons, and, as a result, the PL intensity and the occupation numbers $N_E \leqslant E_{p0}$ of the optically active low-energy states abruptly rise within a few nanoseconds after the trailing edge of the excitation pulse. It is the integrated PL intensity of the indirect excitons that increases after the end of the excitation pulse, and the integrated intensity of all PL above the indirect exciton is negligibly small. This indicates that the rise of the indirect exciton intensity after the excitation pulse end is due to the scattering from optically dark states.

The measured PL kinetics is strongly nonlinear (figures 10(b) and (c)) [25]: the observed increase of τ_{rise}^{-1} with increasing exciton concentration (or W) proves that the scattering is stimulated by the final exciton state occupancy which, in turn, is high, $N_{\mathbf{p} \leqslant \mathbf{p_0}} > 1$. The observed decrease of τ_{rise}^{-1} with increasing temperature (figure 10(d)) results from a thermal reduction of the occupation of the low-energy exciton states $N_{\mathbf{p} \leqslant \mathbf{p_0}}$. The observed decrease of τ_{rise}^{-1} in the presence of a magnetic field (figure 10(e)) is mainly caused by an increase of the magnetoexciton mass $M_X = M_X (B)$, see section 2.4.2 [26, 101]. Figure 11(b) shows that
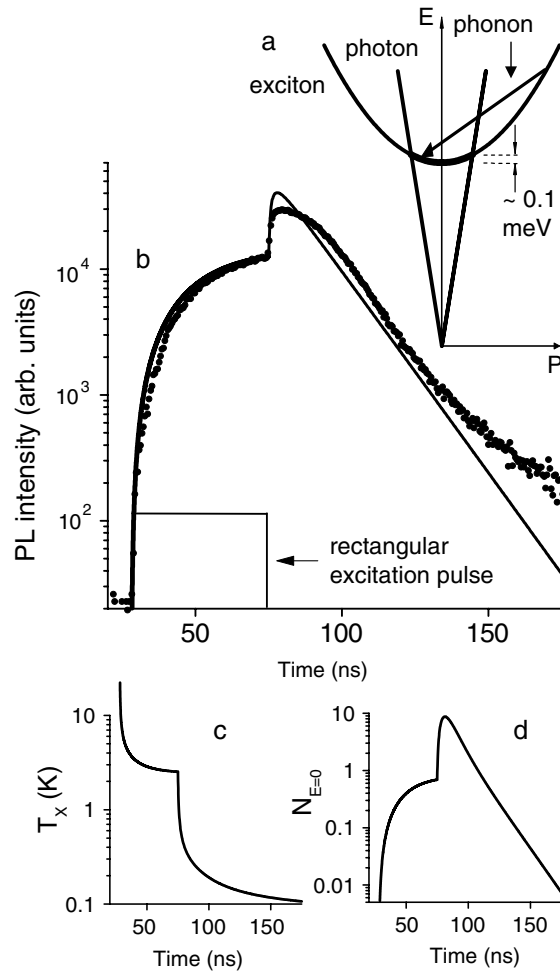
Figure 11. (a) Energy diagram for the LA-phonon-assisted relaxation and optical decay of indirect excitons in GaAs/AlGaAs CQWs. The bold sector of the parabolic exciton dispersion indicates the radiative zone for indirect excitons. The calculated dynamics of (b) the PL intensity of indirect excitons $I_{\text{PL}}(t)$, (c) the effective exciton temperature $T_{\text{X}}(t)$, and (d) the ground-state occupation number $N_{E=0}(t)$ (lines). The parameters used in the numerical modelling refer to the experimental PL kinetics observed at $W = 10\,\text{W\,cm}^{-2}$, $T_{\text{b}} = 50\,\text{mK}$, $B = 0$ and shown in (b) by points. From [25, 29].

the numerical simulations reproduce the observed PL dynamics. According to the calculations plotted in figure 11(c), the end of the excitation pulse is indeed accompanied by a sharp drop of T_{X}. According to figure 11(d), the PL jump after the pump pulse is accompanied by $N_{E=0} \gg 1$, i.e. a strongly degenerate Bose-gas of indirect excitons builds up.

3.3. Photoluminescence lineshape analysis

The exciton condensation is expected to be accompanied by a change of the exciton PL line shape which reflects the distribution of excitons over the exciton states (with a weight proportional to the radiative recombination probability of the state). In particular, the exciton
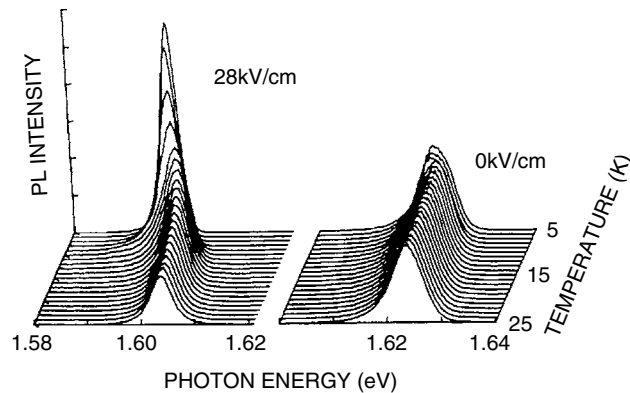
Figure 12. Temperature dependence of the PL spectra at 0 and 28 kV cm^{-1}. From [52].

condensation in homogeneous media is expected to result in a sharp PL peak on the lower energy side of the exciton PL spectrum corresponding to the emission of the macroscopically occupied state. The enhancement of PL intensity at low energies compared to that for the Maxwell–Boltzmann exciton distribution [64, 123] and the appearance of the sharp peak on the lower energy in the exciton PL spectra [96] were discussed in terms of the Bose–Einstein distribution of excitons and the exciton condensation in Cu$_2$O. However, the data on the PL lineshape in Cu$_2$O were explained quantitatively by the spatial inhomogeneity of classical exciton gas [111, 112, 142, 113] as mentioned in section 1.

The analysis of PL lineshape in QWs (or CQWs) is even more complicated due to in-plane potential fluctuations (see section 2.3): the spatially integrated PL lineshape of excitons in QWs (or CQWs) is mainly determined by the random potential and reflects the distribution of excitons over a large number of local potential minima.

A sharp change in the PL lineshape of indirect excitons in CQWs with reducing temperature was observed in [52]: in a narrow temperature interval around $T \approx 5$ K the linewidth dropped from ~ 5–6 meV to ~ 3.5–4 meV (figure 12). The PL lineshape change was interpreted in terms of a phase transition in the exciton system in [52]. However, in the following paper [70] the PL lineshape variation with reducing temperature was re-interpreted in terms of the exciton distribution in the random potential.

The PL lineshape of the indirect excitons in CQWs was also studied in [85–89, 40]. In the experiments of [85–88], the exciton PL integrated over a large excitation spot was studied. In these experiments, in a narrow temperature interval around $T \approx 5$ K the exciton linewidth dropped from ~ 3.5–4 meV to ~ 1.5–2 meV; the narrower PL line at lower temperatures developed on the high-energy side of the broader PL line at higher temperatures. The line narrowing was accompanied by a drastic increase in the degree of circular polarization of the exciton PL and a significant increase of the exciton radiative decay rate (as mentioned in section 3.1). The PL lineshape variation was interpreted in terms of the collective behaviour of indirect excitons and the exciton condensation [85–88].

In the subsequent experiments [89, 40] the surfaces of the samples were coated with an opaque metal mask containing windows of μm size for the photoexcitation and observation of PL. The substantial reduction of the excitation spot by the window reduced drastically the number of local potential minima which were detected in the experiment. Considerably more pronounced narrowing of the exciton PL line was reported under these conditions compared to the experiments without the mask [52, 70, 85–88]: in a narrow temperature interval the exciton
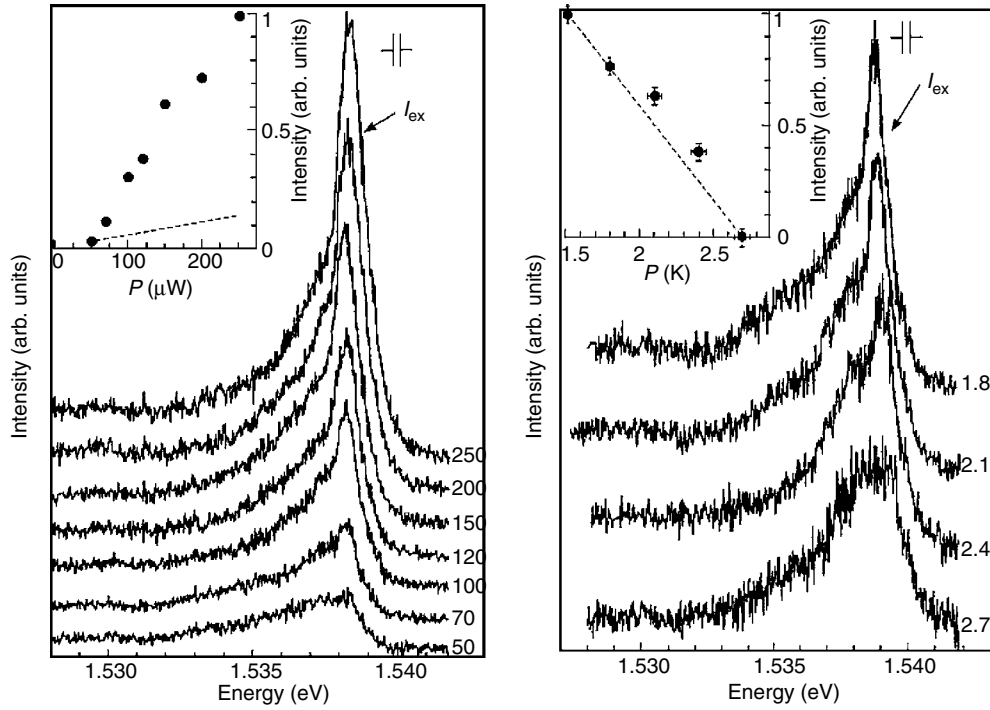
Figure 13. (left) Photoluminescence spectra of the inter-well exciton (I_{ex} line) under conditions of resonance excitation of the direct 1s HH exciton for various excitation powers, bias $U = 0.3$ V and $T = 1.51$ K. The numbers to the right of the spectra indicate the excitation power in μW. The spectral resolution of the instrument is shown at the top right. Inset: the IWE line intensity (dots) versus optical excitation power. The dashed line is the extrapolation of the linear dependence of the background intensity. (Right) Temperature dependence of the IWE line intensity for the excitation power $P = 150\,\mu$W and the bias $U = 0.3$ V. The numbers to the right indicate the temperature in K. Dots in the inset show the temperature behaviour of the IWE line intensity, and the dashed line is the extrapolation of the $I_T \propto (1-T/T_c)$ dependence. From [89].

linewidth dropped from $\sim$2.5 meV to less than 1 meV (the narrowest reported linewidth was 0.35 meV); the narrower PL line at lower temperatures developed on the high energy side of the broader PL line at higher temperatures, figure 13 [89, 40]. The PL lineshape variation was interpreted in terms of the Bose condensation of the indirect excitons [89, 40]. The critical temperature for the phenomenon observation was found to increase with increasing excitation power as $P^{2/3}$ in the interval $T = 0.5$–3.6 K [40].

Note that in all the experiments on indirect excitons reported so far the PL linewidths considerably exceed the temperatures (see e.g. figures 3, 12, 13). Surprisingly, this does not compromise the sharp changes of the variety of parameters reviewed in the sections above at temperatures which are considerably lower than the indirect exciton PL linewidth. Understanding the origin of the PL lineshape (and the broad linewidth) of the indirect excitons remains a challenging problem for future studies.

4. Pattern formation in exciton systems

In this section, we briefly review spatially resolved PL experiments revealing a pattern formation in the exciton system.
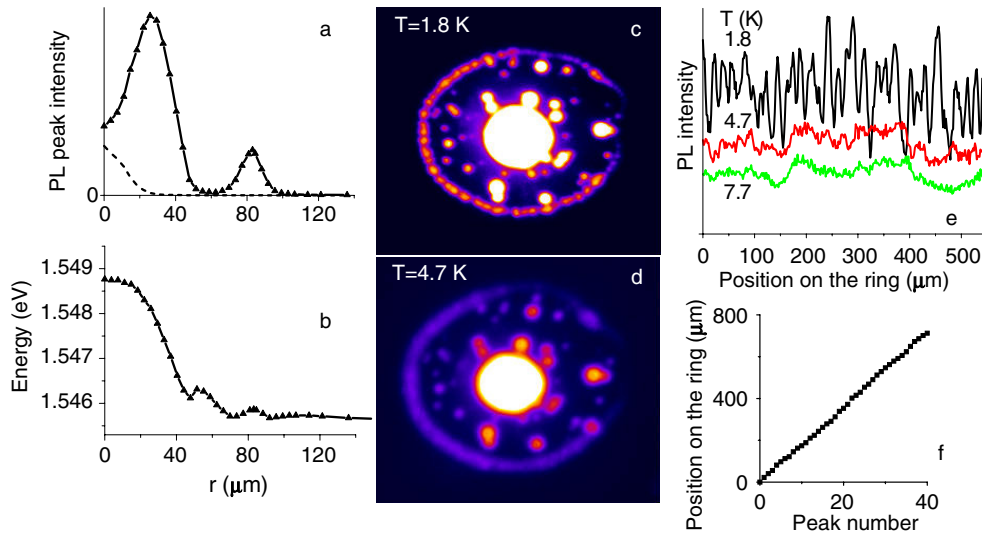
Figure 14. (a) Peak intensity and (b) energy of the indirect exciton PL versus r, the distance from the excitation spot centre, at $T = 1.8$ K, and the excitation power $P_{ex} = 390 \,\mu$W. The excitation spot profile is shown by the dashed line in (a). Spatial pattern of the indirect exciton PL intensity at $T = 1.8$ (c) and 4.7 K (d) for $P_{ex} = 690 \,\mu$W. The area of view is $475 \times 414 \,\mu$m. (e) The corresponding variation of the indirect exciton PL intensity along the external ring at $T = 1.8$, 4.7, and 7.7 K. The dependence of the position of the indirect exciton PL intensity peaks along the external ring versus the peak number is nearly linear (f), showing that the fragments form a periodic chain. From [28, 29].

At the lowest excitation powers, P_{ex}, the spatial profile of the indirect exciton PL intensity, practically follows the laser excitation intensity. However, at high P_{ex}, the indirect exciton PL pattern is characterized by a ring structure: the laser excitation spot is surrounded by two concentric bright rings separated by an annular dark inter-ring region (figure 14a) [28]. The rest of the sample outside the external ring is dark. The internal ring appears near the edge of the laser excitation spot and its radius reaches tens of μm. The external ring can be remote from the excitation spot by more than 100 μm. Its radius increases with P_{ex}. The ring structure follows the laser excitation spot when it is moved over the whole sample area. When the temperature is increased, the bright rings wash out gradually and the PL profile approaches a monotonic bell-like shape [28].

The spatial pattern shows also that the indirect exciton PL intensity is strongly enhanced in certain fixed spots on the sample called localized bright spots (LBS), figure 14(c) [28]. For any excitation spot location and any P_{ex} the LBS are only observed when they are within the area terminated by the external ring, figure 14(c). In the LBS the indirect exciton PL line is spectrally narrow, FWHM ≈ 1.2 meV.

The external ring is fragmented into circular-shape structures that form a periodic array over macroscopic lengths, up to ~ 1 mm (figures 14(c) and (e)). This is demonstrated in figure 14(f), which shows the nearly linear dependence of the fragment positions along the ring versus their number. The in-plane potential fluctuations are not strong enough to destroy the ordering (figure 14(f)). The fragments follow the external ring either when the excitation spot is moved over the sample area or when the ring radius varies with P_{ex}. Along the whole external ring, both in the peaks and the passes, the indirect exciton PL lines are spectrally narrow with the full-width at half-maximum ≈ 1.3 meV, considerably smaller than at the centre

of the excitation spot. The ring fragmentation into the periodic chain appears abruptly at low temperatures below ~ 2 K; this is quantified by the amplitude of the Fourier transform of the PL intensity variation along the ring (figure 18(c)). Each fragment contains a macroscopic number of excitons which can exceed tens of thousands and the period of the fragmentation varies within the macroscopic length scale, 10–50 μm. We call the exciton state with spatial order on macroscopic length scale the macroscopically ordered exciton state [28].

The features observed in the exciton PL pattern [28] include the inner rings, the external rings, the localized bright spots, and the macroscopically ordered exciton state. One of the features—the external ring—has been reproduced: soon after the ring observation was published in [28] a paper reporting the observation of a similar ring in other CQW materials was submitted [125]. Both in [28] and in [125] the ring was observed up to high temperatures: up to ~ 10 K in [28] and up to ~ 100 K in [125] where no exciton degeneracy is expected (see section 1). Note that in [125] the ring was observed up to temperatures ~ 100 K which exceed the binding energy of the indirect excitons by about two times and therefore practically no excitons exist at these high temperatures due to the exciton dissociation to free electrons and holes. However, in [125] it was speculated that the ring is strongly related to the exciton BEC. The observation of the ring at high temperatures where no exciton degeneracy is expected and even at temperatures where essentially no excitons exist makes the interpretation of the ring in terms of the exciton BEC inconsistent. The external ring was also observed in single QWs [119].

4.1. Exciton rings

We now discuss the origin of the observed effects. Under cw photoexcitation, there is a continuous flow of excitons out of the excitation spot owing to the exciton diffusion, drift, phonon wind, etc [28]. (Note that ballistic transport of excitons out of the excitation spot at supersonic velocity for hundreds of μm was discussed in [126, 127]; there is no experimental indication for such ballistic transport of excitons for hundreds of μm.) The exciton diffusion originates directly from the exciton density gradient. The exciton drift also originates from the density gradient as the latter results in the gradient of the indirect exciton potential energy because of the repulsive interaction (figure 14(b)). As the excitons travel away from the excitation spot, T_X decreases with increasing radial distance owing to the energy relaxation of the excitons. The reduction of T_X leads to an enhancement of the radiative zone occupation (see section 3.2) and, therefore, increases the PL intensity; this mechanism can account for the inner ring of radius up to tens of μm observed around the excitation spot [28]. Within this mechanism the excitons travel in a dark state after having been excited, until slowed down to a velocity below the photon emission threshold, where they can decay radiatively [47, 60, 4, 38, 34, 8].

While this mechanism was initially speculated to contribute also to the external ring formation [28], within this framework, a number of qualitative features of the external ring appear to be difficult to explain. In particular, why are the rings so sharp, why does the ring radius change with gate voltage, and why do rings produced by several excitation spots interact before overlapping?

To that end, we were led to assume that the excitons are generated at the ring [31]. Most of the hot electrons and holes, created by the off-resonance excitation [28], cool down and form excitons giving rise to PL observed within or near the laser spot. However, charge neutrality of the carriers excited in the CQW by an off-resonance laser excitation is generally violated, mainly due to electrons and holes having different collection efficiency to the CQW [147]. Overall charge neutrality in the sample is maintained by opposite charge accumulating
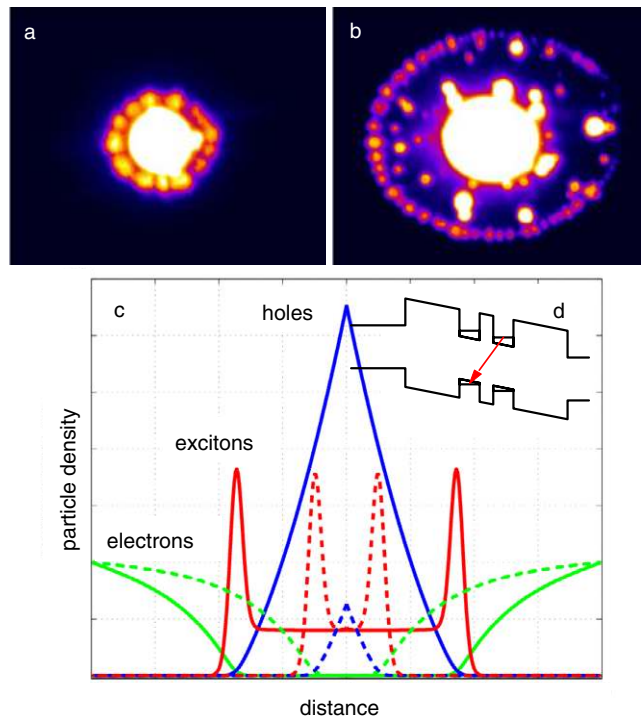
Figure 15. Exciton rings at different photoexcitation intensity: the pattern of indirect exciton PL at $T = 380$ mK and $V_g = 1.24$ V for (a) $P_{ex} = 310\,\mu$W and (b) $P_{ex} = 930\,\mu$W. The excitation spot size is $\sim 30\,\mu$m. The area of view is $410 \times 330\,\mu$m. (c) The carrier distribution as predicted by the transport model at two excitation intensities (the scales are in au). (d) The CQW band diagram. From [31].

in the doped region outside CQW. We note parenthetically that the sign of carrier imbalance cannot be deduced from first principles. We speculate that the current through CQWs from n-doped GaAs layers (figure 15(d)) creates an electron gas in the CQW, while excess holes are photogenerated in the laser excitation spot due to higher collection efficiency of photoexcited holes to the CQW which are heavier than electrons. However, nothing in the discussion and conclusions below will be affected if electrons are replaced by holes and vice versa.

The holes created at the excitation spot diffuse out and bind with electrons, forming indirect excitons. This process depletes electrons in the vicinity of the laser spot, creating an essentially electron-free and hole-rich region, which allows holes to travel a relatively large distance without encountering electrons. At the same time, a spatial nonuniformity in the electron distribution accumulates, causing a counterflow of electrons towards the laser spot. A sharp interface between the hole-rich region and the outer electron-rich area forms (figure 15(c)), since a carrier crossing into a minority region binds rapidly with an opposite carrier to form an exciton. The origin of the external exciton rings was explained by theories and experiments reported in [31, 119]. In [119] the external rings were observed in single QW. Observation of the external ring up to high temperatures, as high as ~ 10 K in [28] and ~ 100 K in [125], and for direct excitons which are hot due to their short recombination lifetime in [119], is not surprising since the ring is classical and does not require degeneracy in the exciton system [31, 119]. We note that since the ring observation reported in [28] and before the model of

the ring was developed in [31, 119] a possible relationship between the charge imbalance of photoexcited carriers and PL ring patterns has been discussed qualitatively by Igor Kukushkin [82] and by David Snoke *et al* [126, 127].

The mechanism of charge transport can be explored within a simple model in which electrons and holes move in the CQW plane, each species in its own quantum well, governed by the coupled diffusion equations $\partial n / \partial t = D \Delta n - wnp + J(r)$ and $\partial p / \partial t = D' \Delta p - wnp + J'(r)$ with $n(r)$ and $p(r)$ the electron and hole concentrations, D and D' the diffusion constants, and w the rate at which an electron and hole bind to form an exciton. The source term for holes is localized at the excitation spot, $J'(r) = P_{ex} \delta(r)$, while the electron source is spread out over the entire plane, $J(r) = I(r) - a(r)n(r)$, with $I(r)$ and $a(r)n(r)$ the currents in and out of the CQW. The stationary solution of these equations, with spatially independent parameters I and a, displayed in figure 15(c), indeed shows a structure of two regions dominated by electrons and holes, and separated by a sharp interface where the exciton density $n \propto np$ is peaked.

The ring can be externally controlled by gate voltage: reducing the voltage across the structure from $V_g = 1.3$ V to $V_g = 1.262$ V makes the ring expand from $R \approx 180$ to $R \approx 300 \, \mu$m (at $P_{ex} = 1.4$ mW), see [31]. Ring expansion with reducing V_g is consistent with the model since a reduction of transverse electric field, and hence of the current $I(r)$, depletes electrons in the CQWs, while holes in the inner region remain practically unaffected.

Experiments with two rings created by spatially separated laser spots (figures 16(a)–(d)) reveal the most intriguing prediction of the transport model: the carrier distribution is strongly perturbed not only inside, but also outside the ring. As the spots are brought closer, the rings attract one another, deform, and then open towards each other (figures 16(a)–(c)). This happens well before the rings coalesce into a common oval-shaped ring (figure 16(d)), suggesting the existence of 'dark matter' outside the rings that mediates the interaction. In the transport model, which readily accounts for the attraction (figures 16(e)–(g)), this dark matter is just the electron flow outside each ring which is perturbed by the presence of another ring. Electrons in the area between the rings are depleted more strongly than at the same radial distance in other directions, which shifts the balance of carrier fluxes to the hole side. As a result, the electron–hole interface moves further out between the rings. The configuration of the electron–hole interfaces in a stationary state from two hole sources of equal strength at $\mathbf{r} = \mathbf{r}_{1,2}$ is given by a family of Bernoulli lemniscata $|\mathbf{r} - \mathbf{r}_1| \times |\mathbf{r} - \mathbf{r}_2| = $ const (figures 16(e)–(g)).
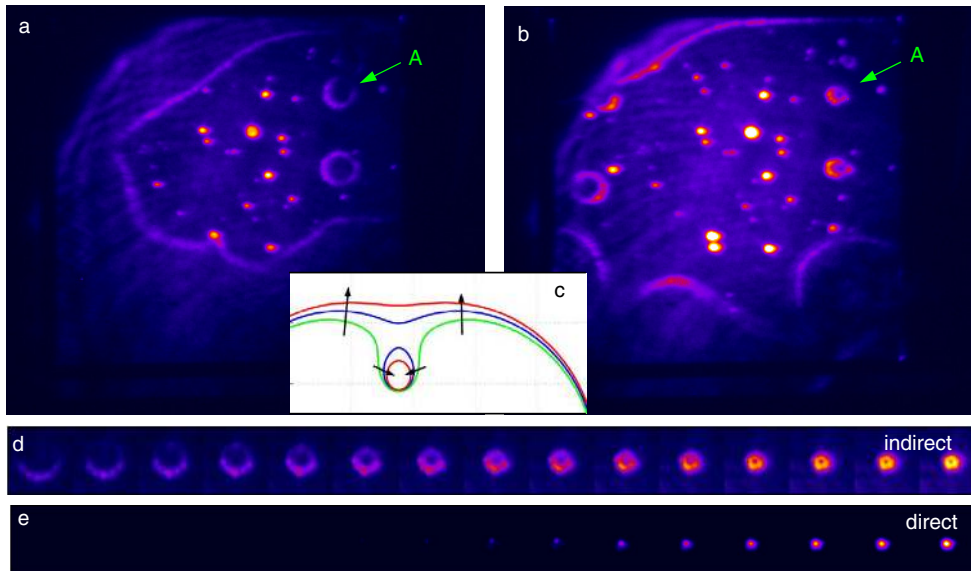
4.2. Localized bright spots

The origin of the localized bright spots was revealed by defocusing the laser excitation source and illuminating a large area (figure 17) [31]. In this excitation geometry, around the localized spots, small rings appear which mirror the behaviour of the outer ring. However, the rings *shrink* at increasing laser power, indicating that the electron–hole contrast here is inverted. This suggests that the spots represent localized sources of electrons (at current filaments crossing CQW) embedded in the hole-rich illuminated area. A model with a bright hole source and a weaker electron source shows the same qualitative behaviour (figure 17(c)). By increasing hole flux (via P_{ex}), as soon as the electron source is enveloped by the hole rich area, a ring forms around it and then starts to shrink. Therefore the LBS were found to be the collapsed rings which are centred at the localized electron sources.

However, a number of interesting properties of the LBS remains unclear at present. In particular, the energy profile of the exciton distribution around the LBS has a minimum at the centre thus resembling a 'potential trap' for the indirect excitons [27]. It is essential that the diameter of the exciton cloud near the bottom of the 'potential trap' reduces as the temperature is lowered while the peak intensity increases as studied in [27, 84]. The shrinkage of the
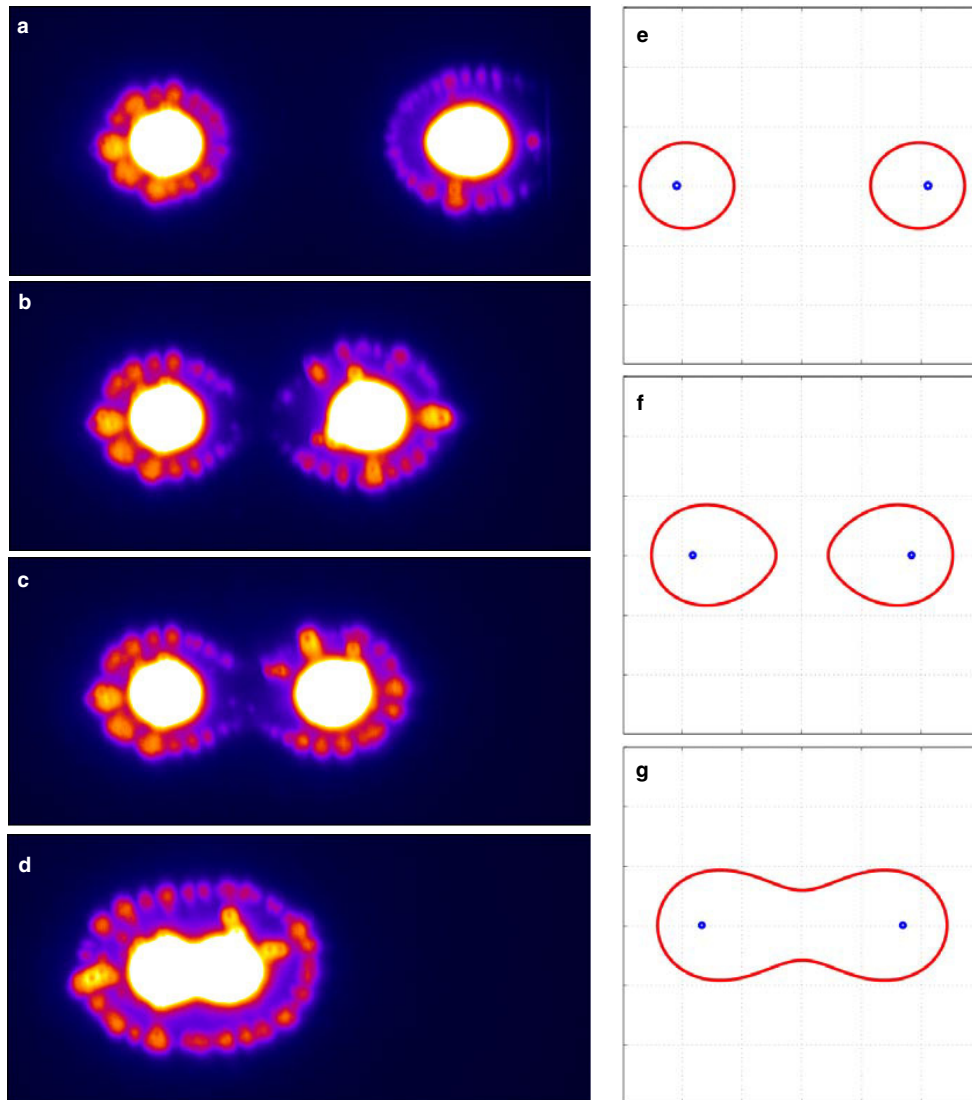
Figure 16. Pattern of indirect exciton PL for two sources at $T = 380$ mK, $V_g = 1.24$ V, and $P_{ex} = 230$ μW per beam for different separations (a)–(d) between the excitation spots. The area of view is 520×240 μm. (e)–(g) Theoretical prediction for the electron–hole interface evolution at decreasing distance between the two point sources (the scales are in au). Note the ring attraction in (b), (c) and (f). From [31].

exciton cloud in the 'potential trap' with reducing temperature leads to effective accumulation of cold and dense exciton gas in the localized spatial region around the 'trap' centre [27]. Note however, that the core of the LBS is hot as indicated by PL of high energy direct exciton emission (figures 17(e) and 18(b)) probably due to the heating by the electron source at the centre. The origin of the trap-like energy profile for the indirect excitons at the localized spots and the origin of the exciton cloud shrinkage with reducing temperature are, at present, unclear. We note that the spatial shrinkage of the exciton cloud in the 'potential traps' is reminiscent

Figure 17. Shrinkage of exciton rings to localized bright spots at nearly homogeneous excitation: spatial PL pattern for indirect excitons at $T = 1.8$ K, $V_g = 1.15$ V, and (a) $P_{ex} = 390\,\mu$W and (b) $P_{ex} = 600\,\mu$W. With (a) and (b), the area of view is $690 \times 590\,\mu$m. (c) Theoretical electron–hole interface for a point source of holes and a weaker point source of electrons. Arrows show interface displacement at increasing hole number. Note the ring shrinking around the electron source. The shrinkage of ring A (a, b) of indirect excitons is detailed in (d) for $T = 380$ mK, $V_g = 1.155$ V and $P_{ex} = 77$–$160\,\mu$W (from left to right) with the defocused excitation spot maximum moved to a location directly below ring A. With (d) and (e), the area of view is $67 \times 67\,\mu$m for each image. Ring shrinkage is accompanied by the onset of the direct exciton emission (e) indicating hot cores at the centre of the collapsed rings. From [31].

of the spatial shrinkage of the atom clouds in the potential traps that is characteristic of atomic BEC. Note however that the spatial shrinkage of the exciton cloud with reducing temperature observed in [27] does not allow one to claim macroscopic occupation of one state, i.e. exciton BEC, in the 'traps'.

4.3. Macroscopically ordered exciton state

The most interesting feature of the PL pattern is ring fragmentation into aggregates forming a highly regular, periodic array over macroscopic lengths of up to 1 mm (figures 14–18) [28, 31]. These aggregates are clearly distinct from the localized bright spots originating from the localized sources of electrons: in contrast to the latter, the aggregates move in concert with the ring when the position of the source is adjusted. Moreover, in contrast to the LBS, the aggregates are *cold*: they do not contain direct excitons (figures 18(a) and (b)).

   The external ring is far from the hot excitation spot and, therefore, the conditions in the ring are optimal for the formation of a very cold exciton gas: the excitons in the ring are formed from well-thermalized carriers and, more importantly, due to the extremely long lifetimes of indirect excitons the binding energy released at exciton formation has little effect on their temperature [31]. The heating source in the external ring—the binding energy released at exciton formation—is the smallest heating source among those accompanying the exciton generation in CQWs: the binding energy of ~ 5 meV is considerably smaller than the energy of hot photoexcited carriers in the excitation spot that is hundreds of meV in the experiments
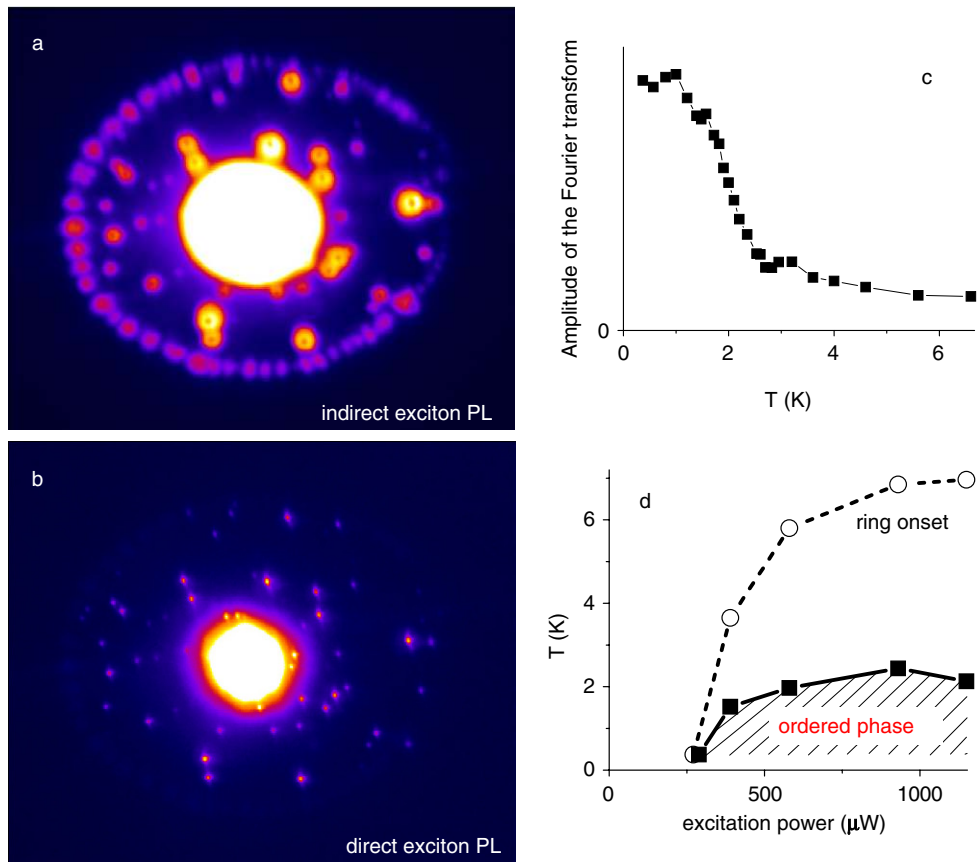
Figure 18. Fragmented ring and localized spots in the (a) indirect and (b) direct exciton PL image. The area of view is $410 \times 340\,\mu$m. Note that the hot cores with high energy direct excitons, present in the localized spots, are absent in the ring fragments. (c) Exciton density Fourier transform peak height at the fragmentation period vanishes continuously at a critical temperature. (d) The phase diagram of the states of the external ring. The phase boundary of the modulated state observed at the lowest experimental temperatures (solid line) along with the ring onset region (dashed line) are marked. From [31].

on exciton pattern formation. (Note that to achieve high density of indirect excitons, general experiments explore the photoexcitation at or above the direct exciton resonance where photon absorption coefficient is high; in these experiments, the energies of the hot photoexcited carriers exceed 20 meV typically, see section 2.1.) The external ring is a region where the excess of the temperature of the system—excitons at low $T_{lattice}$ or electron–hole plasmas at high $T_{lattice}$—over the lattice temperature is the smallest. While the external ring is a classical object by itself (section 4.1) it is the region where the *coldest exciton gas* is created.

Cold exciton temperatures in the ring allow observation of the ordering which appears abruptly as the temperature is decreased below ~ 2 K. The phase diagram, obtained from the PL distribution along the ring (see figures 14(e) and 18(c)), is presented in figure 18(d).

The exciton ring instability and the formation of the macroscopically ordered state have not been predicted. The temperature dependence (figures 18(c) and (d)) indicates that the observed ordering is a low-temperature phenomenon.

We note that spontaneous macroscopic ordering can occur both for quantum (e.g. soliton trains in atom BEC [129]) and classical (e.g. Taylor vortices [132]) systems. The macroscopic ordering is observed in the same temperature range as bosonic stimulation of exciton scattering (section 3.2), below a few K. This implies that the macroscopic ordering could be an intrinsic property of a statistically degenerate Bose-gas of excitons, although it being just a coincidence of the parameters cannot be excluded.

The fragmentation of the exciton system, i.e. formation of higher density exciton clumps (that are qualitatively distinct from the metallic e–h droplets [73]), requires a positive feedback to density variations. An attractive interaction is an example of positive feedback while a repulsive interaction is an example of negative feedback. Indeed, a repulsive interaction suppresses the fragmentation in exciton density as it is energetically unfavourable. In the experiments on atom BEC [129], the stripe of atomic BEC was homogeneous in the case of repulsive interaction and, conversely, was fragmented to the periodic soliton train in the case of attractive interaction due to the modulational instability. Another example, as far from BEC as possible, is gravitational instability, which results in the fragmentation of gaseous slabs and filaments to a periodic array of high-density clumps that is a step towards the formation of stars [32].

An attractive interaction itself is unlikely in the system of indirect excitons (see section 2.2) and, moreover, the experiments show monotonic enhancement of the exciton energy with increasing exciton density in the ring thus suggesting repulsive interaction in the ring (for a discussion of the possibility for attractive interaction in the system of indirect excitons see [29]). The mechanism of positive feedback in the ring that can explain the macroscopically ordered exciton state has been suggested in [95]. Namely, it was shown that the realization of quantum degeneracy in a cold electron/hole–exciton system can result in spatial density modulation due to stimulated kinetics of exciton formation. Qualitatively, the stimulated transition mechanism for hydrodynamic instability can be understood as follows: a local fluctuation in the exciton density leads to an increase in the stimulated electron–hole binding rate. The associated depletion of the local carrier concentration causes neighbouring carriers to stream towards the point of fluctuation presenting a mechanism of positive feedback. The wavelength, determined by the most unstable harmonic of the density, characterizes the length-scale of spatial modulation in the nonuniform state. However, the macroscopically ordered exciton state is a new state which has not been predicted. The origin of this state is, at present, unclear, and should be clarified by further studies.

5. Summary

In this contribution, we reviewed briefly the problem of exciton condensation in CQW semiconductor nanostructures where a cold exciton gas with temperatures below the critical temperature for exciton condensation can be created. We reviewed specific properties of the indirect excitons, experiments that signal exciton condensation in CQWs, and experiments on the recently observed pattern formation in the exciton system. Without going into details, we attempted to overview the current status of studies in this quickly developing field.

Acknowledgments

References

[1] Alexandrou A, Kash J A, Mendez E E, Zachau M, Hong J M, Fukuzawa T and Hase Y 1990 *Phys. Rev.* B **42** 9225
[2] Altshuler B L, Lee P A and Webb R A 1991 *Mesoscopic Phenomena in Solids* ed V M Agranovich and A A Maradudin (Amsterdam: North-Holland)
[3] Andreani L C, Pasquarello A and Bassani F 1987 *Phys. Rev.* B **36** 5887
[4] Andreani L C, Tassone F and Bassani F 1991 *Solid State Commun.* **77** 641
[5] Bagnato V and Kleppner D 1991 *Phys. Rev.* A **44** 7439
[6] Bauer G E W and Ando T 1988 *Phys. Rev.* B **38** 6015
[7] Bayer M, Timofeev V B, Faller F, Gutbrod T and Forchel A 1996 *Phys. Rev.* B **54** 8799
[8] Bjork G, Pau S, Jacobson J and Yamamoto Y 1994 *Phys. Rev.* B **50** 17336
[9] Brusov P N and Popov V N 1988 *Superfluidity and Collective Properties of Quantum Liquids* (Moscow: Nauka) ch 6
[10] Bryant G W 1993 *Phys. Rev.* B **47** 1683
[11] Bulatov A E and Tikhodeev S G 1993 *Phys. Rev.* B **46** 15058
[12] Butov L V, Kulakovskii V D and Andersson T G 1991 *Phys. Rev.* B **44** 1692
[13] Butov L V, Kulakovskii V D, Lach E, Forchel A and Grutzmacher D 1991 *Phys. Rev.* B **44** 10680
[14] Butov L V, Egorov V D, Kulakovskii V D and Andersson T G 1992 *Phys. Rev.* B **46** 15156
[15] Butov L V, Zrenner A, Bohm G and Weimann G 1993 *J. Physique* **IV** 167
[16] Butov L B, Zrenner A, Abstreiter G, Bohm G and Weimann G 1994 *Phys. Rev. Lett.* **73** 304
[17] Butov L V, Zrenner A, Abstreiter G, Petinova A V and Eberl K 1995 *Phys. Rev.* B **52** 12153
[18] Butov L V and Filin A I 1998 *Phys. Rev.* B **58** 1980
[19] Butov L V and Filin A I 1998 *Zh. Eksp. Teor. Fiz.* **114** 1115 (*Sov. Phys.—JETP* **87** 608)
[20] Butov L V, Imamoglu A, Mintsev A V, Campman K L and Gossard A C 1999 *Phys. Rev.* B **59** 1625
[21] Butov L V, Shashkin A A, Dolgopolov V T, Campman K L and Gossard A C 1999 *Phys. Rev.* B **60** 8753
[22] Butov L V, Mintsev A V, Filin A I and Eberl K 1999 *Zh. Eksp. Teor. Fiz.* **115** 1890 (*Sov. Phys.—JETP* **88** 1036)
[23] Butov L V, Mintsev A V, Lozovik Yu E, Campman K L and Gossard A C 2000 *Phys. Rev.* B **62** 1548
[24] Butov L V, Imamoglu A, Campman K L and Gossard A C 2001 *Zh. Eksp. Teor. Fiz.* **119** 301 (*Sov. Phys.—JETP* **92** 260; *Sov. Phys.—JETP* **92** 752)
[25] Butov L V, Ivanov A I, Imamoglu A, Littlewood P B, Shashkin A A, Dolgopolov V T, Campman K L and Gossard A C 2001 *Phys. Rev. Lett.* **86** 5608
[26] Butov L V, Lai C W, Chemla D S, Lozovik Yu E, Campman K L and Gossard A C 2001 *Phys. Rev. Lett.* **87** 216804
[27] Butov L V, Lai C W, Ivanov A L, Gossard A C and Chemla D S 2002 *Nature* **417** 47
[28] Butov L V, Gossard A C and Chemla D S 2002 *Preprint* cond-mat/0204482
     Butov L V, Gossard A C and Chemla D S 2002 *Nature* **418** 751
[29] Butov L V 2003 *Solid State Commun.* **127** 89
[30] Butov L V 2003 *Phys. Status Solidi* b **238** 381
[31] Butov L V, Levitov L S, Simons B D, Mintsev A V, Gossard A C and Chemla D S 2003 *Preprint* cond-mat/0308117
     Butov L V, Levitov L S, Simons B D, Mintsev A V, Gossard A C and Chemla D S 2004 *Phys. Rev. Lett.* **92** 117404
[32] Chandrasekhar S and Fermi E 1953 *Astrophys. J.* **118** 116
[33] Chen X M and Quinn J J 1991 *Phys. Rev. Lett.* **67** 895
[34] Citrin D S 1993 *Phys. Rev.* B **47** 3832
[35] Comte C and Nozieres P 1982 *J. Phys.* **43** 1069
[36] Cornell E A and Wieman C E 2002 *Rev. Mod. Phys.* **74** 875
[37] de-Leon S B-T and Laikhtman B 2001 *Phys. Rev.* B **63** 125306
[38] Deveaud B, Clerot F, Roy N, Satzke K, Sermage B and Katzer D S 1991 *Phys. Rev. Lett.* **67** 2355
[39] Dignam M M and Sipe J E 1991 *Phys. Rev.* B **43** 4084

[40] Dremin A A, Timofeev V B, Larionov A V, Hvam J and Soerensen K 2002 *Pis. Zh. Eksp. Teor. Fiz.* **76** 526 (*JETP. Lett.* **76** 450)
[41] Dynes R C, White A E, Graybeal J M and Garno J P 1986 *Phys. Rev.* B **57** 2195
[42] Dzyubenko A B and Lozovik Yu E 1984 *Fiz. Tverd. Tela* **26** 1540 (*Sov. Phys.—Solid State* **26** 938)
[43] Dzyubenko A B and Bauer G E W 1995 *Phys. Rev.* B **51** 14524
[44] Dzyubenko A B and Yablonskii A L 1996 *Phys. Rev.* B **53** 16355
[45] Elliott R J and Loudon R 1959 *J. Phys. Chem. Solids* **8** 382
[46] Elliott R J and Loudon R 1960 *J. Phys. Chem. Solids* **15** 196
[47] Feldmann J, Peter G, Gobel E O, Dawson P, Moore K, Foxon C and Elliott R J 1987 *Phys. Rev. Lett.* **59** 2337
[48] Fisher D S and Hohenberg P C 1988 *Phys. Rev.* B **37** 4936
[49] Fisher M P A, Weichman P B, Grinstein G and Fisher D S 1989 *Phys. Rev.* B **40** 546
[50] Fortin E, Fafard S and Mysyrowicz A 1993 *Phys. Rev. Lett.* **70** 3951
[51] Fukuzawa T, Kano S S, Gustafson T K and Ogawa T 1990 *Surf. Sci.* **228** 482
[52] Fukuzawa T, Mendez E E and Hong J M 1990 *Phys. Rev. Lett.* **64** 3066
[53] Gold A 1992 *Physica* C **190** 483
[54] Golub J E, Baranovskii S D and Thomas P 1997 *Phys. Rev. Lett.* **78** 4261
[55] Gilliland G D, Antonelli A, Wolford D J, Bajaj K K, Klem J and Bradley J A 1993 *Phys. Rev. Lett.* **71** 3717
[56] Gorbatsevich A A and Tokatly I V 1998 *Semicond. Sci. Technol.* **13** 288
[57] Gor'kov L P and Dzyaloshinskii I E 1967 *Zh. Exp. Teor. Fiz.* **53** 717 (*1968 Sov. Phys.—JETP* **26** 449)
[58] Goto T, Shen M Y, Koyama S and Yokouchi T 1997 *Phys. Rev.* B **55** 7609
[59] Guseinov R R and Keldysh L V 1972 *Zh. Eksp. Teor. Fiz.* **63** 2255 (*1973 Sov. Phys.—JETP* **36** 1193)
[60] Hanamura E 1988 *Phys. Rev.* B **38** 1228
[61] Hasegawa H and Howard R E 1961 *J. Phys. Chem. Solids* **21** 179
[62] Hasuo M, Nagasawa N, Itoh T and Mysyrowicz A 1993 *Phys. Rev. Lett.* **70** 1303
[63] Haviland D B, Liu Y and Goldman A M 1989 *Phys. Rev. Lett.* **62** 2180
[64] Hulin D, Mysyrowicz A and à la Guillaume C B 1980 *Phys. Rev. Lett.* **45** 1970
[65] Imamoglu A 1996 *Phys. Rev.* B **54** R14285
[66] Ivanov A L, Ell C and Haug H 1997 *Phys. Rev.* E **55** 6363
[67] Ivanov A L, Littlewood P B and Haug H 1999 *Phys. Rev.* B **59** 5032
[68] Ivanov A L 2002 *Europhys. Lett.* **59** 586
     Kagan Yu M, lectures, unpublished
[69] Kallin C and Halperin B I 1984 *Phys. Rev.* B **30** 5655
[70] Kash J A, Zachau M, Mendez E E, Hong J M and Fukuzawa T 1991 *Phys. Rev. Lett.* **66** 2247
[71] Keldysh L V and Kopaev Yu E 1964 *Fiz. Tverd. Tela* **6** 2791 (*1965 Sov. Phys.—Solid State* **6** 6219)
[72] Keldysh L V and Kozlov A N 1968 *Zh. Eksp. Teor. Fiz.* **54** 978 (*Sov. Phys.—JETP* **27** 521)
[73] Keldysh L V 1986 *Contemp. Phys.* **27** 395
[74] Ketterle W and Van Drutten N J 1996 *Phys. Rev.* A **54** 656
[75] Ketterle W 2002 *Rev. Mod. Phys.* **74** 1131
[76] Kohn W and Sherrington D 1970 *Rev. Mod. Phys.* **42** 1
[77] Kosterlitz J M and Thouless D J 1973 *J. Phys. C: Solid State Phys.* **6** 1181
[78] Krauth W, Trivedi N and Ceperley D 1991 *Phys. Rev. Lett.* **67** 2307
[79] Krivolapchuk V V, Mazurenko D A, Moskalenko E S, Poletaev N K, Zhmodikov A L, Cheng T S and Foxon C T 1998 *Fiz. Tverd. Tela* **40** 803 (*Phys. Solid State* **5** 737)
[80] Krivolapchuk V V, Moskalenko E S, Zhmodikov A L, Cheng T S and Foxon C T 1999 *Solid State Commun.* **111** 49
[81] Kukushkin I V, V. D. Kulakovskii and Timofeev V B 1981 *JETP Lett.* **34** 34
[82] Kukushkin I V 2002 private communication
[83] Kuramoto Y and Horie C 1978 *Solid State Commun.* **25** 713
[84] Lai C W, Zoch J, Gossard A C and Chemla D S 2004 *Science* **303** 503
[85] Larionov A V, Timofeev V B, Hvam J and Soerensen K 2000 *Pis. Zh. Eksp. Teor. Fiz.* **71** 174 (*JETP Lett.* **71** 117)
[86] Larionov A V, Timofeev V B, Hvam J and Soerensen C 2000 *Zh. Eksp. Teor. Fiz.* **117** 1255 (*JETP* **90** 1093)
[87] Larionov A V and Timofeev V B 2001 *Pis. Zh. Eksp. Teor. Fiz.* **73** 342 (*JETP Lett.* **73** 301)
[88] Larionov A V, Timofeev V B, Hvam J and Soerensen K 2002 *Pis. Zh. Eksp. Teor. Fiz.* **75** 233 (*JETP Lett.* **75** 200)
[89] Larionov A V, Timofeev V B, Ni P A, Dubonos S V, Hvam J and Soerensen K 2002 *Pis. Zh. Eksp. Teor. Fiz.* **75** 689 (*JETP Lett.* **75** 570)

[90] Lee D K K and Gunn J M F 1990 *J. Phys.: Condens. Matter* **2** 7753
[91] Lerner I V and Lozovik Yu E 1978 *Pis. Zh. Eksp. Teor. Fiz.* **27** 467 (*JETP Lett.* **27** 467)
[92] Lerner I V and Lozovik Yu E 1980 *Zh. Eksp. Teor. Fiz.* **78** 1167 (*Sov. Phys.—JETP* **51** 588)
[93] Lerner I V and Lozovik Yu E 1980 *J. Low Temp. Phys.* **38** 333
[94] Lerner I V and Lozovik Yu E 1981 *Zh. Eksp. Teor. Fiz.* **80** 1488 (*Sov. Phys.—JETP* **53** 763)
[95] Levitov L S, Simons B D and Butov L V 2004 *Preprint* cond-mat/0403377
[96] Lin J L and Wolfe J P 1993 *Phys. Rev. Lett.* **71** 1222
[97] Lozovik Yu E and Yudson V I 1976 *Zh. Eksp. Teor. Fiz.* **71** 738 (*Sov. Phys.—JETP* **44** 389)
[98] Lozovik Yu E and Yudson V I 1977 *Pis. Zh. Eksp. Fiz.* **25** 18 (*JETP Lett.* **66** 355)
[99] Lozovik Yu E and Berman O L 1996 *JETP Lett.* **64** 573
[100] Lozovik Yu E and Ruvinskii A M 1997 *Zh. Eksp. Teor. Fiz.* **112** 1791 (*Sov. Phys.—JETP* **85** 979)
[101] Lozovik Yu E, Ovchinnikov I V, Volkov S Yu, Butov L V and Chemla D S 2002 *Phys. Rev.* B **65** 235304
[102] Ma M, Halperin B I and Lee P A 1986 *Phys. Rev.* B **34** 3136
[103] Mysyrowicz A, Benson E and Fortin E 1996 *Phys. Rev. Lett.* **77** 896
[104] Naka N and Nagasawa N 2003 *Phys. Status Solidi* b **238** 397
[105] Negoita V, Snoke D W and Eberl K 1999 *Phys. Rev.* B **60** 2661
[106] Negoita V, Snoke D W and Eberl K 2000 *Phys. Rev.* B **61** 2779
[107] Negoita V, Snoke D W and Eberl K 2000 *Solid State Commun.* **113** 437
[108] Negoita V, Hackworth D, Snoke D and Eberl K 2000 *Opt. Lett.* **25** 572
[109] Nikonov D E and Imamoglu A 1998 *Preprint* quant-ph/9806003
[110] Nozieres P and Comte C 1982 *J. Phys.* **43** 1083
[111] O'Hara K E, Suilleabhain L O and Wolfe J P 1999 *Phys. Rev.* B **60** 10565
[112] O'Hara K E, Gullingsrud J R and Wolfe J P 1999 *Phys. Rev.* B **60** 10872
[113] O'Hara K E and Wolfe J P 2000 *Phys. Rev.* B **62** 12909
[114] Paquet D, Rice T M and Ueda K 1985 *Phys. Rev.* B **32** 5208
[115] Parlangeli A, Cristianen P C M, Maan J C, Tokatly I V, Soerensen C B and Lindelof P E 2000 *Phys. Rev.* B **62** 15323
[116] Popov V N 1972 *Theor. Math. Phys.* **11** 565
[117] Prokof'ev N, Ruebenacker O and Svistunov B 2001 *Phys. Rev. Lett.* **87** 270402
[118] Salmassi B R and Bauer G E W 1989 *Phys. Rev.* B **39** 1970
[119] Rapaport R, Chen G, Snoke D, Simon S H, Pfeiffer L, West K, Liu Y and Denev S 2003 *Preprint* cond-mat/0308150
     Rapaport R, Chen G, Snoke D, Simon S H, Pfeiffer L, West K, Liu Y and Denev S 2004 *Phys. Rev. Lett.* **92** 117405
[120] Reppy J D 1984 *Physica* B **126** 335
[121] Schmitt-Rink S, Chemla D S and Miller D A B 1989 *Adv. Phys.* **38** 89
[122] Shevchenko S I 1976 *Fiz. Nizk. Temp.* **2** 505 (*Sov. J. Low Temp. Phys.* **2** 251)
[123] Snoke D, Wolfe J P and Mysyrowicz A 1987 *Phys. Rev. Lett.* **59** 827
[124] Snoke D W, Wolfe J P and Mysyrowicz A 1990 *Phys. Rev. Lett.* **64** 2543
[125] Snoke D, Denev S, Liu Y, Pfeiffer L and West K 2002 *Nature* **418** 754
[126] Snoke D, Liu Y, Denev S, Pfeiffer L and West K 2003 *Solid State Commun.* **127** 187
[127] Snoke D 2003 *Phys. Status Solidi* b **238** 389
[128] Stern F 1968 *Phys. Rev. Lett.* **21** 1687
[129] Strecker K E, Partridge G B, Truscott A G and Hulet R G 2002 *Nature* **417** 150
[130] Szymanska M H and Littlewood P B 2003 *Phys. Rev.* B **67** 193305
[131] Takagahara T 1995 *Phys. Rev.* B **51** 14524
[132] Taylor G I 1923 *Phil. Trans. R. Soc.* A **223** 289
[133] Tikhodeev S G 1989 *Solid State Commun.* **72** 1075
[134] Tikhodeev S G 1990 *Zh. Eksp. Teor. Fiz.* **97** 681 (*Sov. Phys.—JETP* **70** 380)
[135] Tikhodeev S G 1997 *Phys. Rev. Lett.* **78** 3225
     Mysyrowicz A, Benson E and Fortin E 1997 *Phys. Rev. Lett.* **78** 3226
[136] Tikhodeev S G, Kopelevich G A and Gippius N A 1998 *Phys. Status Solidi* b **206** 45
[137] Timofeev V B, Kulakovskii V D and Kukushkin I V 1983 *Physica* B&C **117–118** 327
[138] Timofeev V B, Larionov A V, Ioselevich A S, Zeman J, Martinez G, Hvam J and Soerensen S 1998 *Pis. Zh. Eksp. Teor. Fiz.* **67** 580 (*JETP Lett.* **67** 613)
[139] Timofeev V B, Larionov A V, Zeman J, Martinez G, Hvam J, Birkedal D and Soerensen S 1998 *Sov. Phys.—Usp.* **41** 109
[140] Timofeev V B, Larionov A V, Alessi M G, Capizzi M, Frova A and Hvam J M 1999 *Phys. Rev.* B **60** 8897

[141] Valles J M Jr, Dynes R C and Garno J P 1992 *Phys. Rev. Lett.* **69** 3567
[142] Warren J T, O'Hara K E and Wolfe J P 2000 *Phys. Rev.* B **61** 8215
[143] White A E, Dynes R C and Garno J P 1986 *Phys. Rev.* B **33** 3549
[144] Yoshioka D and MacDonald A H 1990 *J. Phys. Soc. Japan* **59** 4211
[145] Zhao W, Stenius P and Imamoglu A 1997 *Phys. Rev.* B **56** 5306
[146] Zhu X, Littlewood P B, Hybertsen M and Rice T 1995 *Phys. Rev. Lett.* **74** 1633
[147] Zrenner A, Worlock J M, Florez L T, Harbison J P and Lyon S A 1990 *Appl. Phys. Lett.* **56** 1763
[148] Zrenner A, Leeb P, Schafler J, Bohm G, Weimann G, Worlock J M, Florez L T and Harbison J P 1992 *Surf. Sci.* **263** 496
[149] Zrenner A 1992 *Festkorperprobleme/Adv. Solid State Phys.* **32** ed U Rossler (Braunschweig/Weisbaden: Vieweg) p 61